Automated retrievals of volcanic ash and dust cloud properties from upwelling infrared measurements

Michael J Pavolonis,[1] Andrew K. Heidinger,[1] and Justin Sieglaff[2]

Received 11 October 2012; revised 4 January 2013; accepted 9 January 2013.

[1] A fully automated, globally applicable algorithm to retrieve ash and dust cloud properties from infrared satellite measurements is presented. The algorithm, which will serve as the official operational algorithm of the next generation Geostationary Operational Environmental Satellite (GOES-R), utilizes an optimal estimation framework that allows uncertainties in the measurements and forward model to be taken into account and uncertainty estimates for each of the retrieved parameters to be determined. The retrieval approach is globally applicable because background atmospheric water vapor, surface temperature, and surface emissivity are explicitly accounted for on a pixel-by-pixel basis. The retrieval is demonstrated using the Spinning Enhanced Visible and Infrared Imager (SEVIRI) on-board the Second Generation Meteosat. Ash clouds from the 2010 eruption of Eyjafjallajökull in Iceland and the 2010 eruption of Soufriere Hills in the eastern Caribbean and a Saharan dust cloud were analyzed, and the accuracy of the retrieval was evaluated using spaceborne lidar measurements. The validation analysis shows that the retrieved ash/dust cloud height, cloud emissivity, and effective particle radius generally agrees well with lidar measurements, especially when volcanic ash clouds are assumed to be composed of andesite and dust clouds composed of kaolinite.

Citation: Pavolonis, M. J., A. K. Heidinger, and J. Sieglaff (2013), Automated retrievals of volcanic ash and dust cloud properties from upwelling infrared measurements, *J. Geophys. Res. Atmos.*, *118*, doi:10.1002/jgrd.50173.

1. Introduction

[2] While the aviation impacts of volcanic ash clouds have only recently gained widespread public attention due to the April/May 2010 eruption of Eyjafjallajökull in Iceland, airborne volcanic ash has been considered a major aviation hazard since the early 1980s when a British Airways B747 aircraft lost power to all four engines after flying into a volcanic ash cloud over Indonesia in 1982 [*Miller and Casadevall*, 2000]. A similar incident occurred in 1989 when KLM Flight-867 lost power to all four engines after encountering an ash cloud outside of Anchorage, Alaska [*Casadevall*, 1994]. Fortunately, the pilots of the British Airways and KLM flights narrowly avoided disaster after being able to at restart some or all of the engines after descending thousands of feet (without power) and out of the airspace heavily contaminated by volcanic ash. Volcanic ash clouds can damage aircraft in the following ways [*International Civil Aviation Organization* (*ICAO*), 2007]:

1. The melting temperature of volcanic ash (~1100°C) is such that when ingested into jet engines it melts in the combustion chamber, cools down in the turbine, and deposits on the turbine vanes, which restricts the flow of high pressure combustion gases and can, in the worst case, cause engine failure.
2. Volcanic ash is very abrasive and can sand blast cockpit windows, airframes, and flight surfaces. It can also erode the turbines.
3. Volcanic ash can clog the pitot-static system. An unobstructed pitot-static system is needed to accurately determine airspeed and altitude.
4. Ingestion of volcanic ash into air conditioning and cooling systems leads to contamination of the electrical and avionics units, fuel and hydraulic systems, and cargo-hold smoke detection systems.

[3] The economic impacts of airborne volcanic ash are also significant. For instance, the April and May 2010 eruptions of Eyjafjallajökull [*Gudmundsson et al.*, 2010] in Iceland had an unprecedented impact on aviation in the North Atlantic and Europe, causing over 100,000 flights to be canceled, the economic impact of which is in the billions of dollars (various news reports). The eruption of Mount Redoubt, Alaska in March and April 2009 resulted in the cancelation of hundreds of passenger and cargo flights into and out of Anchorage [Tony Hall, personal comm.]. The 2008 eruptions of Okmok and Kasatochi in Alaska also significantly impacted United States airspace in the North Pacific [*Guffanti et al.*, 2010]. On average, 50–60 volcanoes erupt per year (eruptions can last anywhere from hours to

[1]National Oceanic and Atmospheric Administration Center for Satellite Applications and Research, Madison, Wisconsin, USA.
[2]Cooperative Institute for Meteorological Satellite Studies, Madison, Wisconsin, USA.

Corresponding author: M. J. Pavolonis, National Oceanic and Atmospheric Administration Center for Satellite Applications and Research, 1225 W. Dayton St., Madison, WI 53706, USA. (Mike.Pavolonis@noaa.gov)

©2013. American Geophysical Union. All Rights Reserved
2169-897X/13/10.1002/jgrd.50173

years), 10 or more of which will produce a volcanic cloud that reaches jet aircraft cruising altitudes [*ICAO*, 2007]. Given the tremendous impact on aviation, sophisticated satellite techniques are needed to characterize volcanic ash clouds in near-real time and a better understanding of the physical properties of volcanic ash clouds is needed to improve volcanic ash transport and dispersion forecast models.

[4] Quantitative monitoring of airborne terrestrial dust, which is spectrally similar to volcanic ash throughout much of the infrared spectrum, is also important. Dust plays a role in the complex climate forcing/feedback problem [e.g., *Evan et al.*, 2009; *Prospero and Lamb*, 2003], impacts tropical storm development [*Dunion and Velden*, 2004], influences biogeochemical cycling in the oceans [e.g., *Jickells et al.*, 2005], and possibly impacts air quality at the surface [*Sandstrom and Forsberg*, 2008].

[5] In this paper, satellite-based infrared measurements will be used to retrieve the radiative temperature, emissivity, and a microphysical parameter of volcanic ash and dust clouds (the term "cloud" will be used throughout this paper in lieu of "aerosol layer" or "ash/dust plume"), analogous to the cirrus cloud retrievals performed by *Heidinger and Pavolonis* [2009] and *Heidinger et al.* [2010]. From these retrieved parameters, the cloud radiative height, effective particle radius, optical depth, and mass loading can be derived, subject to certain assumptions. The retrieval methodology was developed in preparation for the next generation of Geostationary Operational Environmental Satellite (GOES-R) and will serve as the official operational volcanic ash algorithm for GOES-R [*Pavolonis and Sieglaff*, 2010]. The retrieval approach (hereafter referred to as the GOES-R approach), which has already been demonstrated in real-time (http://cimss.ssec.wisc.edu/goes_r/proving-ground/geocat_ash/) and used to support operations at the Anchorage and Washington Volcanic Ash Advisory Centers (VAACs), is unique in that it is fully automated, computationally efficient, globally applicable, explicitly accounts for major absorbing background atmospheric gases, and allows the effective cloud temperature to be a free parameter in the retrieval. The cloud radiative temperature has been treated as a constant in nearly all published imaging radiometer-based volcanic ash retrieval studies [e.g., *Wen and Rose*, 1994; *Prata and Grant*, 2001; *Gu et al.*, 2003; *Zhang et al.*, 2006; *Corradini et al.*, 2008; *Clarisse et al.*, 2010]. In addition, like *Yu et al.* [2002] and *Corradini et al.* [2008], the GOES-R algorithm does not rely on the presence of the traditional "reverse absorption" signal (negative 11–12 μm brightness temperature difference) [*Prata*1989a, 1989b]. A traditional "reverse absorption" signal need not be present because major background absorbing gases (e.g., H_2O, CO_2, and O_3) are accounted for explicitly. The GOES-R approach does not depend on scene dependent offline look-up tables, so it can easily be implemented operationally. Comparisons to other published methodologies like those of *Wen and Rose* [1994], *Prata and Grant* [2001], *Corradini et al.* [2008], *Clarisse et al.,* [2010], *Francis et al.* [2012], and Prata and *Prata* [2012] are valuable and will be performed in a subsequent paper. This paper will focus on describing and justifying the GOES-R ash/dust retrieval methodology and physical basis [*Pavolonis and Sieglaff*, 2010]. Further, as in *Heidinger and Pavolonis* [2009], spaceborne lidar measurements will be used to quantify the accuracy of the retrieval method presented in this paper.

2. Infrared Measurements

[6] Although the basic methodology described in this paper applies to aircraft measurements of upwelling infrared radiation, we will focus on satellite-based infrared measurements, which are generally better suited for global operational monitoring of volcanic ash and dust than research aircraft measurements. Three spectral channels centered near 11, 12, and 13.3 μm will be used to retrieve the ash and dust cloud properties. *Heidinger et al.* [2010] use this same channel combination to retrieve cirrus cloud properties and these channels are not sensitive to SO_2, which simplifies the retrieval (e.g., fewer unknowns) when SO_2 is present, as may be the case in volcanic ash clouds. While the specific spectral characteristics of the channels will differ slightly from sensor to sensor, the channels considered in this paper have approximate central wavelengths of 11, 12, and 13.3 μm and are available on current sensors such as the Moderate Resolution Imaging Spectroradiometer (MODIS) and the Spinning Enhanced Visible/Infrared Imager (SEVIRI) and will be available on all next generation geostationary sensors such as the GOES-R Advanced Baseline Imager (ABI) [*Schmit et al.*, 2005]. Geostationary satellites, because of their high temporal refresh, are critical for monitoring volcanic ash and dust clouds. While certain instruments in low earth orbit have better spectral and/or spatial resolution, the temporal resolution is poor relative to geostationary satellites. It should be noted that the 11 and 12 μm channel combination has been historically used to retrieve the optical depth and effective particle radius of volcanic ash and dust clouds [e.g., *Wen and Rose*, 1994; *Prata and Grant*, 2001; *Yu et al.*, 2002; *Gu et al.*, 2003; *Corradini et al.*, 2008]. However, *Heidinger et al.* [2010] showed that, for cirrus clouds, the addition of the 13.3 μm channel adds considerable sensitivity to the cloud radiative temperature. Although the retrieval approach described in this paper can be applied to hyperspectral infrared measurements (available on certain low earth orbit satellites), more advanced retrieval procedures can be applied to hyperspectral measurements [e.g., *Huang et al.*, 2004; *Peyridieu et al.*, 2010; *Clarisse et al.*, 2010; *DeSouza-Machado et al.*, 2010] so this paper is focused on more commonly available narrow band radiometer measurements. The algorithm described in this paper will be demonstrated using SEVIRI, which is a 12-channel imaging radiometer with a spatial resolution of 3 km (in the infrared at nadir) and is located in a geostationary orbit with a coverage area that includes many volcanoes. For more information on SEVIRI, see http://www.eumetsat.int/. More specifically, volcanic ash from the 2010 eruptions of Eyjafjallajokull (Iceland) and Soufriere Hills (Caribbean) and airborne dust lofted from the Sahara Desert will be used to illustrate algorithm results and co-located spaceborne lidar data will be used to objectively assess algorithm performance.

3. Infrared Radiative Transfer Theory

[7] Assuming a satellite viewing perspective (e.g., upwelling radiation), a fully cloudy field of view, a non-scattering atmosphere (no molecular scattering), and a negligible contribution from downwelling cloud emission or molecular emission that is reflected by the surface and transmitted to the top of troposphere (*Zhang and Menzel* [2002] showed

that this term is very small at infrared wavelengths), the cloudy radiative transfer equation for a given infrared channel or wavelength can be written as in equation (1) [e.g., *Heidinger and Pavolonis*, 2009; *Pavolonis*, 2010]:

$$R_{\mathrm{obs}}(\lambda) = \varepsilon_{\mathrm{eff}}(\lambda)R_{\mathrm{cld}}(\lambda) + R_{\mathrm{clr}}(\lambda)(1 - \varepsilon_{\mathrm{eff}}(\lambda)) \quad (1)$$

[8] While sub-pixel cloudiness is noted as a potential source of error, only fully cloudy fields of view are considered in this paper since information on cloud fraction is not readily available. For a cloud fraction sensitivity analysis, see *Heidinger and Pavolonis* [2009]. In equation (1), which is derived by *Pavolonis* [2010] in Appendix A, λ is wavelength, R_{obs} is the observed radiance, and R_{clr} is the clear sky radiance. The effective cloud emissivity [*Cox*, 1976] is denoted by $\varepsilon_{\mathrm{eff}}$. The effects of cloud scattering are implicitly captured by the effective cloud emissivity (see *Cox* [1976]). To avoid using additional symbols, the angular dependence is simply implied. R_{cld} is given by equation (2):

$$R_{\mathrm{cld}}(\lambda) = R_{\mathrm{ac}}(\lambda) + t_{\mathrm{ac}}(\lambda)B(\lambda, T_{\mathrm{eff}}) \quad (2)$$

[9] In equation (2), R_{ac} and t_{ac} are the above cloud upwelling atmospheric radiance and transmittance, respectively. B is the Planck function, and T_{eff} is the effective cloud temperature. The effective cloud temperature is most often different from the thermodynamic cloud top temperature since the emission of radiation originates from a layer in the cloud. The depth of this layer depends upon the cloud extinction profile, which is generally unknown. The clear sky transmittance and radiance terms are determined using surface temperature, atmospheric temperature, water vapor, and ozone profiles from the Global Forecast Model (GFS) [*Hamill et al.*, 2006], surface emissivity from the Seebor database [*Seemann et al.*, 2008], the satellite zenith angle, and a regression based clear sky radiative transfer model [*Hannon et al.*, 1996]. The procedure for determining the clear sky radiance and transmittance is the same as described in *Heidinger and Pavolonis* [2009], *Heidinger et al.* [2010], and *Pavolonis* [2010], so no other details are given here.

[10] The spectral variation of the effective cloud emissivity is directly related to cloud microphysical information (e.g., particle size, shape, and composition). Effective absorption optical depth ratios, otherwise known as β-ratios, have been previously used to extract cloud microphysical information from infrared measurements [*Inoue*1987; *Parol et al.*, 1991; *Giraud et al.*, 1997; *Heidinger and Pavolonis*, 2009; and *Pavolonis*2010]. For a given pair of spectral effective emissivities, $\varepsilon_{\mathrm{eff}}(\lambda_1)$ and $\varepsilon_{\mathrm{eff}}(\lambda_2)$, the effective absorption optical depth ratio, β_{obs}, is defined in equation (3):

$$\beta_{\mathrm{obs}} = \frac{\ln[1 - \varepsilon_{\mathrm{eff}}(\lambda 1)]}{\ln[1 - \varepsilon_{\mathrm{eff}}(\lambda 2)]} = \frac{\tau_{\mathrm{abs,eff}}(\lambda 1)}{\tau_{\mathrm{abs,eff}}(\lambda 2)} \quad (3)$$

[11] Notice that equation (3) can simply be interpreted as the ratio of effective absorption optical depth ($\tau_{\mathrm{abs,eff}}$) at two different wavelengths. An appealing quality of β_{obs} is that it can be interpreted in terms of the single scatter properties, which can be computed for a given cloud composition and particle distribution. Following *Van de Hulst* [1980] and *Parol et al.* [1991], a spectral ratio of scaled extinction coefficients can be calculated from the single scatter properties (single scatter albedo, asymmetry parameter, and extinction cross-section), as follows.

$$\beta_{\mathrm{theo}} = \frac{[1.0 - \omega(\lambda 1)g(\lambda 1)]\sigma_{\mathrm{ext}}(\lambda 1)}{[1.0 - \omega(\lambda 2)g(\lambda 2)]\sigma_{\mathrm{ext}}(\lambda 2)} \quad (4)$$

[12] In equation (4), β_{theo} is the spectral ratio of scaled extinction coefficients, ω is the single scatter albedo, g is the asymmetry parameter, and σ_{ext} is the extinction cross section. At wavelengths in the 8–15 μm range, where multiple scattering effects are small, β_{theo}, captures the essence of the cloudy radiative transfer such that, as shown in *Pavolonis* [2010]:

$$\beta_{\mathrm{obs}} \approx \beta_{\mathrm{theo}} \quad (5)$$

[13] Equation (5) allows β_{obs} to be used to infer information on cloud particle distribution. In addition, equations (1)–(5) allow for an efficient retrieval without the need for large, scene-dependent, look-up tables.

4. Retrieval Forward Model

[14] Following equation (1), the infrared radiative transfer equation is shown for each spectral channel used in the retrieval in equations (6)–(8):

$$R_{\mathrm{obs}}(11\,\mu\mathrm{m}) = \varepsilon_{\mathrm{eff}}(11\,\mu\mathrm{m})R_{\mathrm{cld}}(11\,\mu\mathrm{m}) + R_{\mathrm{clr}}(11\,\mu\mathrm{m})(1 - \varepsilon_{\mathrm{eff}}(11\,\mu\mathrm{m})) \quad (6)$$

$$R_{\mathrm{obs}}(12\,\mu\mathrm{m}) = \varepsilon_{\mathrm{eff}}(12\,\mu\mathrm{m})R_{\mathrm{cld}}(12\,\mu\mathrm{m}) + R_{\mathrm{clr}}(12\,\mu\mathrm{m})(1 - \varepsilon_{\mathrm{eff}}(12\,\mu\mathrm{m})) \quad (7)$$

$$R_{\mathrm{obs}}(13.3\,\mu\mathrm{m}) = \varepsilon_{\mathrm{eff}}(13.3\,\mu\mathrm{m})R_{\mathrm{cld}}(13.3\,\mu\mathrm{m}) + R_{\mathrm{clr}}(13.3\,\mu\mathrm{m})(1 - \varepsilon_{\mathrm{eff}}(13.3\,\mu\mathrm{m})) \quad (8)$$

[15] The algorithm is designed to directly retrieve the 11 μm effective cloud emissivity and β_{obs}(12/11 μm), in addition to T_{eff}, so equation (3) is used to express the 12 μm effective cloud emissivity as a function of the 11 μm effective cloud emissivity and β_{obs}(12/11 μm), as shown in equation (9):

$$\varepsilon_{\mathrm{eff}}(12\,\mu\mathrm{m}) = 1 - [1 - \varepsilon_{\mathrm{eff}}(11\,\mu\mathrm{m})]^{\beta_{\mathrm{obs}}(12/11\,\mu\mathrm{m})} \quad (9)$$

[16] Similarly the 13.3 μm effective cloud emissivity can be expressed as a function of the 11 μm effective cloud emissivity and β_{obs}(13.3/11 μm), as shown in equation (10).

$$\varepsilon_{\mathrm{eff}}(13.3\,\mu\mathrm{m}) = 1 - [1 - \varepsilon_{\mathrm{eff}}(11\,\mu\mathrm{m})]^{\beta_{\mathrm{obs}}(13.3/11\,\mu\mathrm{m})} \quad (10)$$

[17] The single scatter properties (recall equations (4) and (5)) are then used to relate β_{obs}(12/11 μm) to β_{obs} (13.3/11 μm) such that only T_{eff}, $\varepsilon_{\mathrm{eff}}$(11 μm) and β_{obs} (12/11 μm) are solved for in the retrieval. More specifically, β_{obs}(13.3/11 μm) is related to β_{obs}(12/11 μm) via a fourth-order polynomial fit (see equation (11)) to the single scatter property-derived beta relationship (β_{theo}(13.3/11 μm) versus β_{theo}(12/11 μm)). The polynomial coefficients (c0, c1, c2, c3, and c4) are a function of the microphysical model chosen, and will be discussed in a later section.

$$\beta(13.3/11\,\mu\text{m}) = c4[\beta(12/11\,\mu\text{m})]^4 + c3[\beta(12/11\,\mu\text{m})]^3 + c2[\beta(12/11\,\mu\text{m})]^2 + c1[\beta(12/11\,\mu\text{m})] + c0 \tag{11}$$

5. Optimal Estimation Retrieval Method

[18] The retrieval of T_{eff}, $\varepsilon_{\text{eff}}(11\,\mu\text{m})$ and $\beta_{\text{obs}}(12/11\,\mu\text{m})$ is formally performed using the optimal estimation approach described by *Rodgers* [1976]. *Heidinger and Pavolonis* [2009] utilize this same technique to retrieve cirrus cloud properties. In addition, *Turner* [2008] uses optimal estimation to retrieve dust cloud properties from ground-based infrared measurements. There are many more examples of optimal estimation being used in satellite remote sensing applications. The benefits of this approach are that it is flexible and allows new observations or retrieved parameters to be added or removed from the retrieval scheme. Another benefit of this approach is that it generates estimates of the uncertainty in the retrieval. Each step in the optimal estimation iteration changes each element of vector of retrieved parameters (T_{eff}, $\varepsilon_{\text{eff}}(11\,\mu\text{m})$ and $\beta_{\text{obs}}(12/11\,\mu\text{m})$) according to the following relationship:

$$\delta\mathbf{x} = \mathbf{S_x}\left\{\mathbf{K}^T\mathbf{S_y}^{-1}[\mathbf{y} - f(\mathbf{x})] + \mathbf{S_a}^{-1}(\mathbf{x_a} - \mathbf{x})\right\} \tag{12}$$

[19] In equation (12), $\mathbf{y}$ is the vector of observations, $\boldsymbol{x}$ is the vector of retrieved parameters, $f(\mathbf{x})$ represents the forward model, which is a function of $\mathbf{x}$, and $\mathbf{x}_a$ is the a priori representation of $\mathbf{x}$. The matrices $\mathbf{S}_x$, $\mathbf{S}_y$, and $\mathbf{S}_a$ are the error covariance matrices of the retrieved parameters, the measurements, and the a priori values, respectively. The kernel matrix, $\mathbf{K}$, contains the forward model Jacobians. In our retrieval, $\boldsymbol{x} = [T_{\text{eff}}, \varepsilon(11\,\mu\text{m}), \beta_{\text{obs}}(13.3/11\,\mu\text{m})]$. Using "BT" to denote brightness temperature and "BTD" to denote brightness temperature difference, the observation vector, $\mathbf{y}$ is [BT(11 μm), BTD(11–12 μm), BTD(11–13.3 μm)]. The forward model vector, $f(\mathbf{x})$, is constructed in the same manner as $\mathbf{y}$ for each of the channel combinations. The kernel matrix is defined in equation (13).

$$\mathbf{K} = \begin{pmatrix} \frac{\partial BT(11\mu m)}{\partial Teff} & \frac{\partial BT(11\mu m)}{\partial \varepsilon eff(11\mu m)} & \frac{\partial BT(11\mu m)}{\partial \beta obs(12/11\mu m)} \\ \frac{\partial BTD(11-12\,\mu\text{m})}{\partial T\text{eff}} & \frac{\partial BTD(11-12\,\mu\text{m})}{\partial \varepsilon\text{eff}(11\,\mu\text{m})} & \frac{\partial BTD(11-12\,\mu\text{m})}{\partial \beta\text{obs}(12/11\,\mu\text{m})} \\ \frac{\partial BTD(11-13.3\,\mu\text{m})}{\partial T\text{eff}} & \frac{\partial BTD(11-13.3\,\mu\text{m})}{\partial \varepsilon\text{eff}(11\,\mu\text{m})} & \frac{\partial BTD(11-13.3\,\mu\text{m})}{\partial \beta\text{obs}(12/11\,\mu\text{m})} \end{pmatrix} \tag{13}$$

[20] Given our choice of forward model, analytical expressions for the Jacobians can be derived. The Jacobian analytical expressions can be found in Appendix A. Once the kernel matrix has been calculated, the error covariance matrix of $\mathbf{x}$ can be determined using equation (14) [*Rodgers*, 1976]. The method used to determine $\mathbf{S}_a$ and $\mathbf{S}_y$ will be described shortly.

$$\mathbf{S_x} = \left(\mathbf{S_a}^{-1} + \mathbf{K}^T\mathbf{S_y}^{-1}\mathbf{K}\right)^{-1} \tag{14}$$

[21] The optimal estimation approach is run until the following convergence criterion is met:

$$\left\|\sum \delta\mathbf{x}\mathbf{S}\mathbf{x}^{-1}\delta\mathbf{x}\right\| \le \frac{p}{2} \tag{15}$$

[22] Where p is the size of $\mathbf{x}$, which is 3 in our case. This convergence criterion is the same used by *Rodgers* [1976]. If the retrieval does not converge after 10 iterations, it is deemed a failed retrieval (retrievals very rarely fail to converge) and all retrieved parameters are set to the a priori values. Further, $\delta\mathbf{x}$ is constrained such that the maximum allowed absolute changes in the retrieved parameters, T_{eff}, $\varepsilon(11\,\mu\text{m})$, and $\beta(12/11\,\mu\text{m})$, are 20.0 K, 0.3, 0.2, respectively. Once the retrieval vector is updated by $\delta\mathbf{x}$, the retrieved parameters are constrained to be within a physically plausible range.

[23] The a priori values and their associated uncertainties act to constrain the retrieved parameters when the measurements contain little or no information on one or more of the retrieved parameters. However, prior, independent, knowledge of ash and dust cloud properties is generally not available and climatological values are not very useful since ash and dust cloud properties are highly variable in space and time. Thus, a large uncertainty is assigned to each a priori parameter, so that the measurements are highly weighted. Ideally, ash cloud property estimates from more accurate (but less frequent) measurements (satellite or otherwise) would be used to automatically determine the a priori values and uncertainties. However, combining measurements from different satellites or measurement platforms is not a trivial endeavor and will be the subject of future research. Model simulated ash cloud properties can also potentially be used as a first guess, but quantifying model errors is a difficult task and requires significant additional research. The a priori values and associated uncertainty estimates are shown in Table 1. The choice of a priori value for T_{eff} and $\varepsilon(11\,\mu\text{m})$ assumes that most ash and dust clouds are semi-transparent to infrared radiation and accounts for the satellite zenith angle. The a priori value of $\beta(12/11\,\mu\text{m})$ is chosen as 0.8, which, as will be shown in the next section, approximately corresponds to the center of the range of sensitivity for effective particle size. The actual a priori values, however, are not critically important since the a priori error estimates ($\sigma_{\mathbf{x_ap}}$) are assumed to be significant (see Table 1). As in *Heidinger and Pavolonis* [2009], the a priori error covariance matrix (equation (16)) is taken to be diagonal (e.g., errors in the first guess of each parameter are uncorrelated). The procedure for assigning the a priori values and uncertainty will be refined in the future.

$$\mathbf{S}_a = \begin{pmatrix} \sigma^2{}_{T\text{eff_ap}} & 0.0 & 0.0 \\ 0.0 & \sigma^2{}_{\varepsilon(11\,\mu\text{m})_\text{ap}} & 0.0 \\ 0.0 & 0.0 & \sigma^2{}_{\beta(12/11\,\mu\text{m})_\text{ap}} \end{pmatrix} \tag{16}$$

Table 1. First Guess Values and Associated Uncertainties of Each Retrieved Parameter[a]

Retrieved Parameter ($\boldsymbol{x}$)	First Guess ($\mathbf{x}$_ap)	First Guess Uncertainty (σ^2_{ap})
T_{eff}	BT(11 μm) − 15 K	$(50\,\text{K})^2$
$\varepsilon_{\text{eff}}(11\,\mu\text{m})$	$1.0 - \exp(-0.5/\cos(\theta_{\text{sat}}))$	$(1.0)^2$
$\beta_{\text{obs}}(12/11\,\mu\text{m})$	0.8	$(0.6)^2$

[a] θ_{sat} is the satellite zenith angle.

Table 2. Instrument and Forward Model Errors for Each Observation Used in the Retrieval

Observation	Instrument Error	Clear Sky Error (Water) (σ_{clr})	Clear Sky Error (land) (σ_{clr})
(**y**)	(σ_{instr})		
BT(11 μm)	$(0.11\,K)^2$	$(0.50\,K)^2$	$(5.00\,K)^2$
BTD(11–12 μm)	$(0.26\,K)^2$	$(0.25\,K)^2$	$(1.00\,K)^2$
BTD(11–13.3 μm)	$(0.55\,K)^2$	$(1.50\,K)^2$	$(4.00\,K)^2$

[24] The optimal estimation procedure also requires an estimate of the error covariance matrix of the forward model (equation (17)). As in *Heidinger and Pavolonis* [2009], the total uncertainty in the forward model is assumed to be composed of a linear combination of three major sources (see equation (18)): instrumental, clear sky radiative transfer modeling, and pixel heterogeneity. In equation (18), the instrument uncertainty is given by σ^2_{instr}, the clear sky radiative transfer uncertainty is denoted by σ^2_{clr}, and the uncertainty due to pixel heterogeneity is given by σ^2_{hetero}. The impact of the clear sky radiative transfer uncertainty is approximately inversely proportional to the cloud emissivity, so it is weighted by the 11 μm cloud emissivity, ε(11 μm). As discussed in *Heidinger and Pavolonis* [2009], the off-diagonal elements (correlated uncertainty) of the forward model error covariance matrix are very difficult to determine, so only the diagonal elements (uncorrelated uncertainty) are considered. The uncertainty in the clear sky radiative transfer (σ^2_{clr}), which is a function of the accuracy of the radiative transfer model, the GFS fields, and the surface emissivity database, is determined through an offline clear sky radiance bias analysis, separately for land and water surfaces [see *Heidinger and Pavolonis*, 2009] In general, there is much greater uncertainty in land surface temperature than sea surface temperature so the clear sky uncertainty over land is greater than over water. The forward model uncertainty due to spatial heterogeneity (σ^2_{hetero}) is approximated by the spatial variance of each observation used in the retrieval over a 3 x 3 pixel box centered on the current pixel of interest. The last forward model error term is that due to instrumental effects, σ^2_{instr}. This term includes noise, calibration, and spectral response errors that impact the ability of the forward model to fit the measurements. The clear sky and instrument uncertainty estimates for SEVIRI are given in Table 2. The instrumental uncertainty was taken from satellite operator, EUMETSAT (http://www.eumetsat.int/idcplg?IdcService=GET_FILE&dDocName=PDF_MSG_SEVIRI_RADIOM_NOISE&RevisionSelectionMethod=LatestReleased).

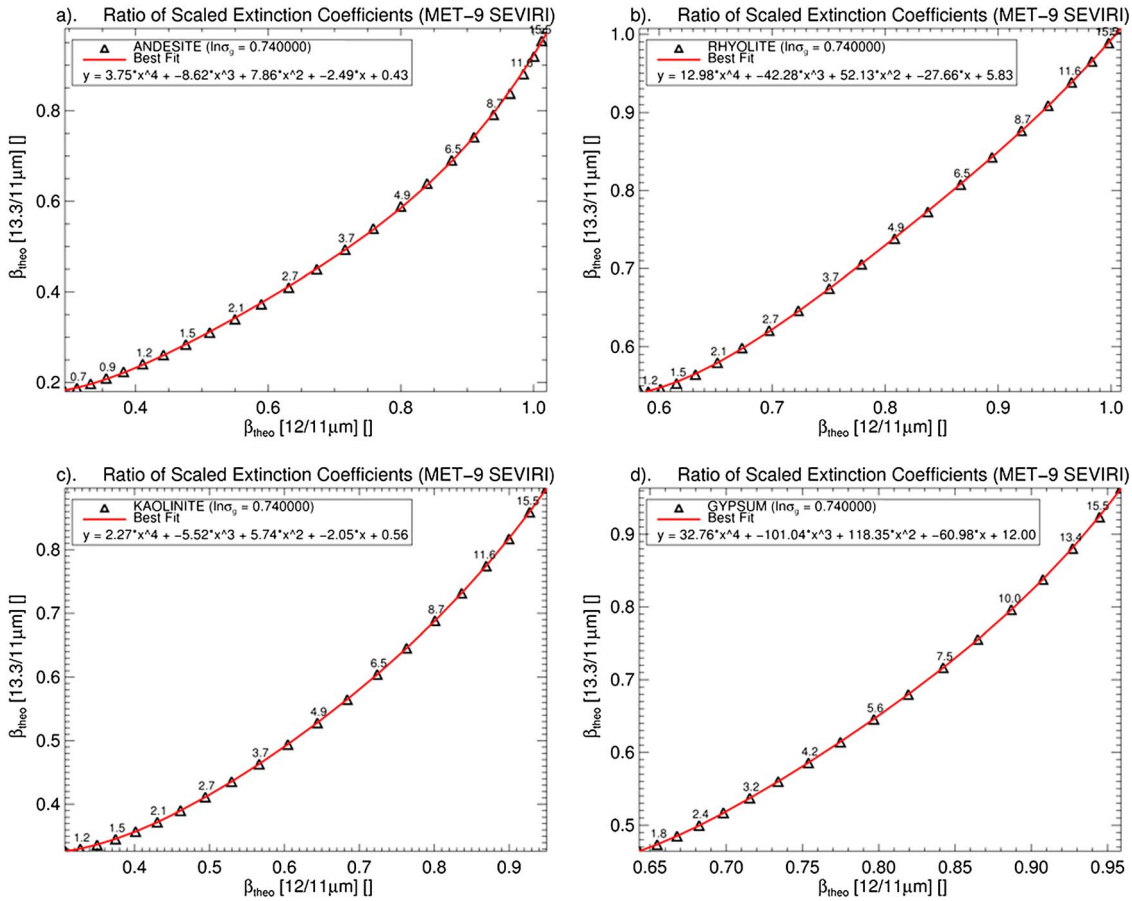

Figure 1. The black triangles show the 13.3/11 μm scaled extinction ratio (β_{theo}(13.3/11 μm)) as a function of the 12/11 μm scaled extinction ratio (β_{theo}(12/11 μm)) for four different mineral compositions over a range of effective radii (1–15 μm). A fourth-order polynomial fit is shown in red. The numbers adjacent to the triangles indicate the effective radius in μm. Also shown are (a) andesite, (b) rhyolite, (c) kaolinite, and (d) gypsum. β_{theo}(12/11 μm) and β_{theo}(13.3/11 μm) were derived from the single scatter properties as described in the text.

$$\mathbf{S_y} = \begin{pmatrix} \sigma^2{}_{BT(11\,\mu m)} & 0.0 & 0.0 \\ 0.0 & \sigma^2{}_{BTD(11-12\,\mu m)} & 0.0 \\ 0.0 & 0.0 & \sigma^2{}_{BTD(11-13.3\,\mu m)} \end{pmatrix} \quad (17)$$

$$\sigma^2 = \sigma^2{}_{\text{instr}} + [1 - \varepsilon(11\,\mu m)]\sigma^2{}_{\text{clr}} + \sigma^2{}_{\text{hetero}} \quad (18)$$

6. Microphysical Models

[25] The microphysical relationships needed to determine $\beta_{\text{obs}}(13.3/11\,\mu m)$ from the retrieved $\beta_{\text{obs}}(12/11\,\mu m)$ (see equation (11)) and to calculate the effective particle radius [*Hansen and Travis*, 1974] and mass loading from the retrieved $\varepsilon_{\text{eff}}(11\,\mu m)$ and $\beta_{\text{obs}}(12/11\,\mu m)$ were constructed for four different mineral compositions: andesite, rhyolite, gypsum, and kaolinite. *Pollack et al.* [1973] provided the indices of refraction for andesite and rhyolite and *Roush et al.* [1991] provided the indices of refraction of the other mineral compositions. Regardless of the mineral composition, the size distribution was assumed to be lognormal:

$$n(r) = \frac{No}{\sqrt{2\pi}} \frac{1}{r ln\sigma_g} exp\left(-\frac{(lnr - lnr_g)^2}{2(ln\sigma_g)^2}\right) \quad (19)$$

where N_o is the total number of particles, r is particle radius, r_g is the geometric mean radius, and σ_g is the geometric standard deviation. In this study, the geometric standard deviation is always set to 2.1 ($\ln(\sigma_g) = 0.74$). Lognormal distributions with a geometric standard deviation of ~2 have commonly been used to model and fit volcanic ash and dust particle distributions [e.g., [*Hobbs et al.*, 1991; *Wen and Rose*, 1994; *Pavolonis et al.*, 2006; *Prata and Grant*, 2001; *Pavolonis*, 2010; *Clarisse et al.*, 2010]. The geometric radius, r_g, can be determined from the effective particle radius [*Hansen and Travis*, 1974], r_{eff}, using

$$r_g = \frac{r_{eff}}{\exp\left(\frac{5}{2}\left(\ln\sigma_g\right)^2\right)} \quad (20)$$

[26] The total number of particles per unit area, N_o, can be calculated from the retrieved effective cloud emissivity, ε_{eff} (11 μm), and $\beta_{\text{obs}}(12/11\,\mu m)$ using

$$No = \frac{\tau(11\,\mu m)}{\sigma_{\text{ext}}(11\,\mu m)} \quad (21)$$

where $\tau(11\,\mu m)$ is the effective cloud optical depth at 11 μm and $\sigma_{\text{ext}}(11\,\mu m)$ is the extinction cross section at 11 μm. The effective cloud optical depth, corrected for satellite viewing zenith angle, θ_{sat}, is easily computed from the retrieved effective cloud emissivity as

$$\tau(11\,\mu m) = -\cos(\theta_{\text{sat}}) \ln[1.0 - \varepsilon(11\,\mu m)] \quad (22)$$

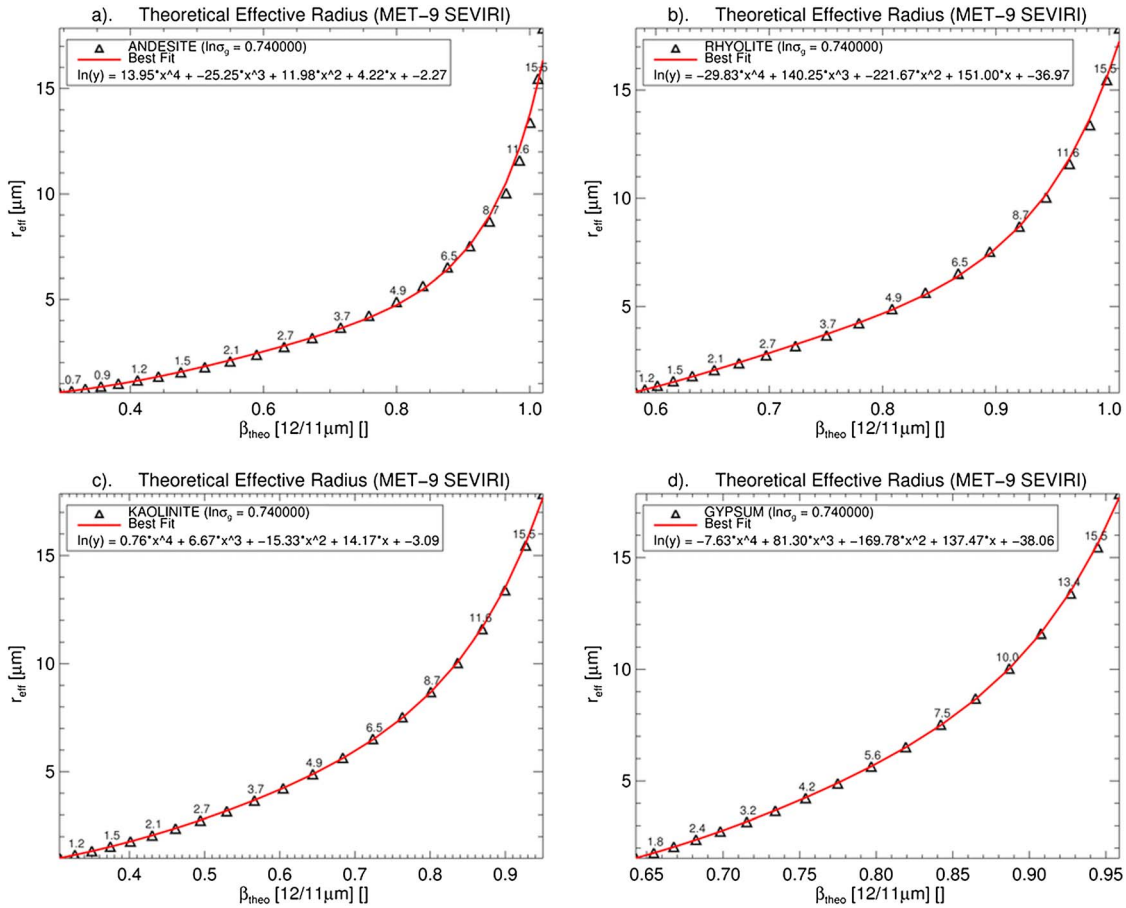

Figure 2. The same as Figure 1 except the effective particle radius (r_{eff}) is shown as a function of $\beta_{\text{theo}}(12/11\,\mu m)$.

[27] As will be shown, the single scatter properties can be expressed as a function of β_{theo}(12/11 μm), which allows σ_{ext}(11 μm) to be determined.

[28] The ash and dust particles were assumed to be spherical and Mie theory is used to compute the single scatter properties for each mineral composition over a range of effective radii (0.5–20.0 μm). Of course, real volcanic ash and dust particles actually take on a variety of irregular shapes that are very difficult to model. Fortunately, in the infrared (especially at wavelengths larger than 10 μm), the sensitivity to particle habit and composition has been shown to be much smaller than the sensitivity to particle size [*Wen and Rose*, 1994; *Corradini et al.* (2008); *Clarisse et al.*, 2010; *Newman et al.*, 2012], so, as in other studies, the particles are treated as spheres. The Mie calculations in the wavelength range of 8–15 μm are performed with a wave number spacing of 10 cm^{-1}. Instrument-specific single scatter properties for each channel required by the retrieval algorithm are compiled by integrating over the corresponding instrument-specific spectral response functions for those channels.

[29] For a given mineral composition, the theoretical beta relationship (equation (4)) over a range of effective radii is used to derive the empirical coefficients needed to evaluate equation (11). Figure 1 shows β_{theo}(13.3/11 μm) as a function of β_{theo}(12/11 μm) for each mineral composition. The coefficients required by equation (11) are determined by fitting a fourth-order polynomial to the points. The relationships shown in Figure 1 are valid for the SEVIRI sensor onboard the Met-9 satellite. The relationship between β_{theo}(12/11 μm) and β_{theo}(13.3/11 μm) has the same primary attribute, β_{theo}(12/11 μm) > β_{theo}(13.3/11 μm) for a given r_{eff}, for all mineral compositions. In an analogous manner, β_{obs} (12/11 μm) is also used to determine the effective particle radius (r_{eff}) and the 11 μm extinction cross-section (σ_{ext} (11 μm)). Those relationships are shown for each mineral composition in Figures 2 and 3, respectively. The empirical relationships depicted in Figures 2 and 3 are valid for Met-9 SEVIRI, but empirical fits of the same general form are used for other instruments. Thus, polynomial coefficients for each instrument of interest are computed and stored in a data file and a single version of the retrieval code is used for all instruments that meet the channel requirements.

[30] Figure 2 shows that the sensitivity to effective radius is generally greatest in the 1–6 μm range (e.g., relatively large changes in β_{theo}(12/11 μm) are associated with relatively small changes in r_{eff}). Once the r_{eff} exceeds ~15 μm, relatively small changes in β_{theo}(12/11 μm) are associated with larger changes in r_{eff} and retrievals of r_{eff} greater than 15 μm cannot be performed reliably. It is also more difficult to separate ash/dust clouds from liquid water and ice clouds when r_{eff} exceeds 15 μm [*Pavolonis*, 2010]. Thus, the maximum allowed retrieved r_{eff} in the GOES-R

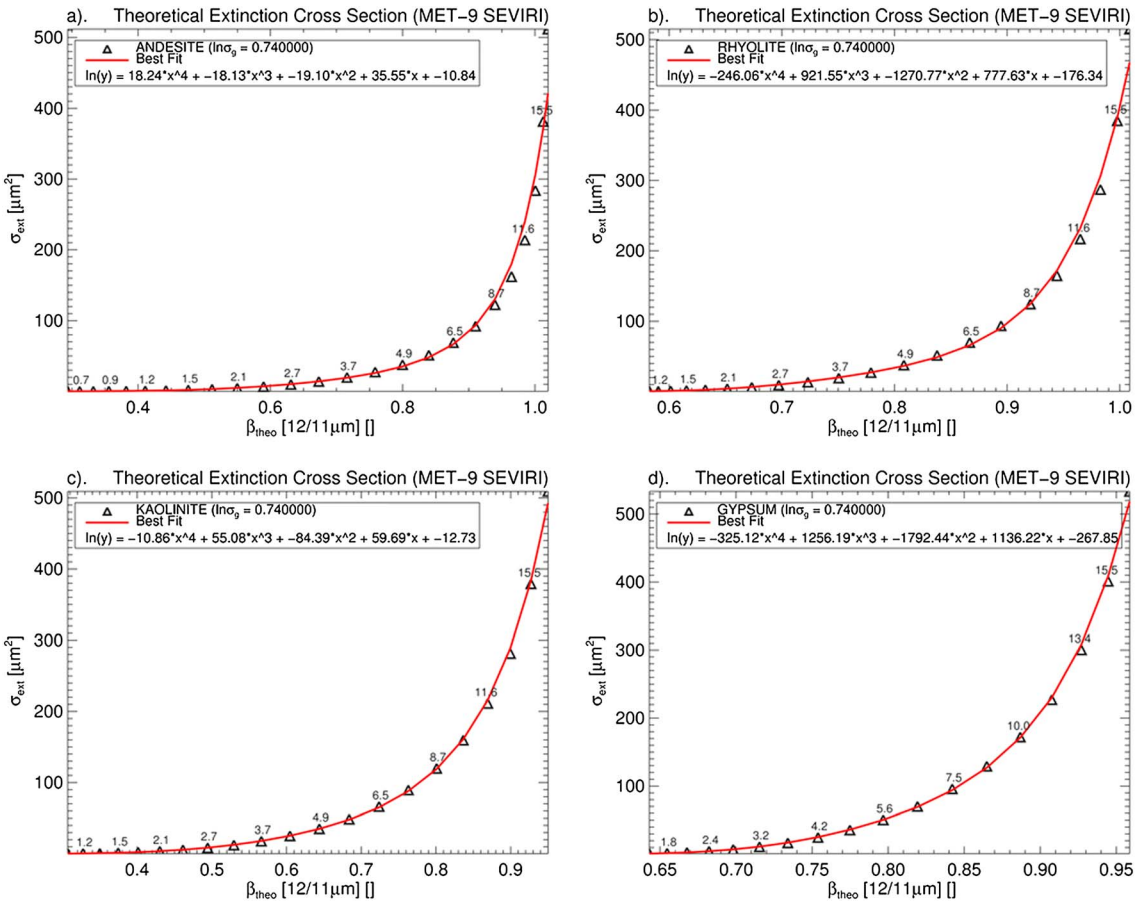

Figure 3. The same as Figure 1 except the extinction cross-section (σ_{ext}) is shown as a function of β_{theo} (12/11 μm).

approach is 15 μm. This does not mean that a volume of particles with an actual $r_{\mathrm{eff}} > 15$ μm does not contribute to the measured top of atmosphere radiation. Figure 3 shows that particles of all sizes greater than about 1 μm have a non-trivial extinction coefficient. In fact, the larger the effective radius, the greater the extinction of radiation. While fundamental (given the physical relationship between particle size and wavelength), this is an important point to make in this paper since the lack of sensitivity to effective radii larger than about 15 μm is sometimes misinterpreted to mean that larger particles within a size distribution do not significantly contribute to the measured radiance in the infrared, which is not correct. The infrared cloud optical depth is greatly influenced by emission and scattering from larger particles.

[31] As in previous studies, ash mass loading in g/m^2 is computed using

$$ML = \left(1 \times 10^6\right) \frac{4}{3} \pi \rho_{\mathrm{ash}} \int_{r1}^{r2} r^3 n(r) dr \tag{23}$$

[32] where ML is the mass loading in tons/km^2 and ρ_{ash} is the density of ash, which is taken to be 2.6 g/cm^3 [*Neal et al.*, 1994]. The particle radius, r, is expressed in units of μm. The units of $n(r)$ are the number of particles per μm^2 per μm. The factor, 1×10^6, in equation (23), is needed to convert the units to g/m^2. Given that the maximum effective radius that can be retrieved is 15 μm, the mass loading will likely be underestimated if the actual effective radius exceeds 15 μm simply because the number of larger volume particles will be underestimated.

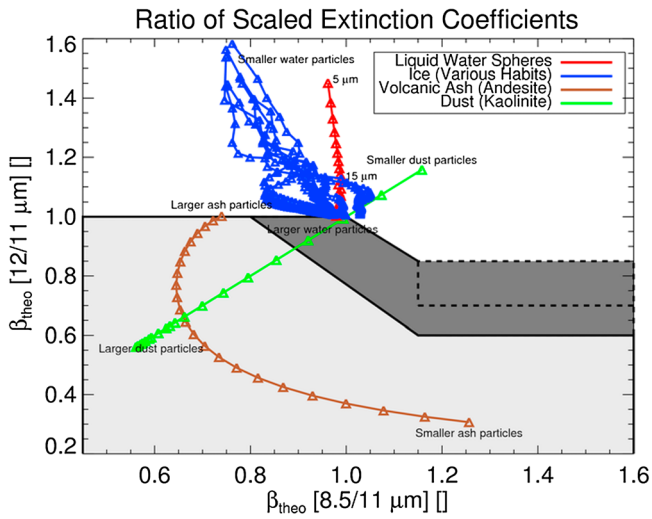

Figure 4. Adapted from Figure 3 of *Pavolonis* [2010], the 12/11 μm scaled extinction ratio (β_{theo}(12/11 μm)) is shown as a function of the 8.5/11 μm scaled extinction ratio (β_{theo}(8.5/11 μm)) for different cloud compositions (liquid water, ice with various non-spherical habits, andesite, and kaolinite) over a range of effective radii. Unlike the figure in *Pavolonis* [2010], areas potentially consistent with volcanic ash and dust clouds are shaded in gray. The lighter gray area indicates additional confidence that the joint occurrence of β_{theo}(8.5/11 μm) and β_{theo}(12/11 μm) is consistent with ash and dust relative to the darker gray area. The dashed box indicates the area where an additional constraint is needed. See *Pavolonis* [2010] and text for additional details.

7. Ash Detection

[33] Prior to performing the optimal estimation retrieval, satellite pixels that likely contain volcanic ash or dust must be identified. Volcanic ash and dust pixels are identified using effective absorption optical depth ratios (β-ratios). *Pavolonis* [2010] first proposed using β-ratios (see equation (3)) for detecting ash and dust clouds in the absence of independent information on cloud height. As is described in detail by *Pavolonis* [2010], β-ratios for the 12/11 μm and 8.5/11 μm channel pairings are computed using the top of troposphere cloud height assumption. Unlike traditional brightness temperature differences, β-ratios provide a means to account for radiation emitted by the surface and major absorbing atmospheric gases. Thus, volcanic ash and dust can be detected even in moist atmospheres where the traditional 11–12 μm brightness temperature difference [*Prata*, 1989a; 1989b] can fail [e.g., *Pavolonis et al.*, 2006]. At this time, volcanic ash and dust clouds can only be detected if liquid water or ice clouds do not overlap them (from a satellite viewing perspective). A modified version of Figure 3 from *Pavolonis* [2010] is shown in Figure 4. This version of the figure includes lines that define different ash/dust confidence regions as a function of β(12/11 μm) and β(8.5/11 μm) computed using equation (3) with the top of troposphere cloud height assumption described in detail in *Pavolonis* [2010]. The top of troposphere cloud height assumption is used since the cloud height is not known prior to performing the retrieval. Volcanic ash and dust are detected using the following logic. All pixels with a top of troposphere 11 μm cloud emissivity [see *Pavolonis*, 2010] greater than T_{emiss} that fall within any of the gray shaded regions in Figure 4 and have an observed BTD(11–12 μm) minus the calculated clear sky BTD(11–12 μm) less than −0.5 K [e.g., *Francis et al.*, 2012] are sorted into cloud objects. The variable threshold, T_{emiss}, is set to 0.10 within the box outlined by the dashed line and 0.02 outside of the dashed line box, where, in practice, there is less spectral overlap between ash/dust and liquid water and ice clouds. A cloud object is defined as a collection of spatially connected pixels that satisfy certain criteria. The method of *Wielicki and Welch* [1986] is used to construct cloud objects. All cloud objects that contain at least one pixel that falls within the region shaded in light gray in Figure 4 are classified as a volcanic ash/dust cloud; otherwise all of the pixels in the cloud object are discarded. As shown in the next section, this method works well for the cases studied in this paper and does not rely on the observed BTD (11–12 μm) being less than 0 K. Under clear sky conditions, the β-ratios will generally be invalid. Thus, the results the ash detection procedure can also be used to determine where ash/dust was not detected under cloudy conditions (meaning ash/dust may be present but is obscured by liquid water and/or ice clouds). When applied globally, this method, like all published ash/dust detection methods, will produce some false alarms and miss some ash/dust clouds. A more sophisticated, globally applicable, ash/dust detection method is under development.

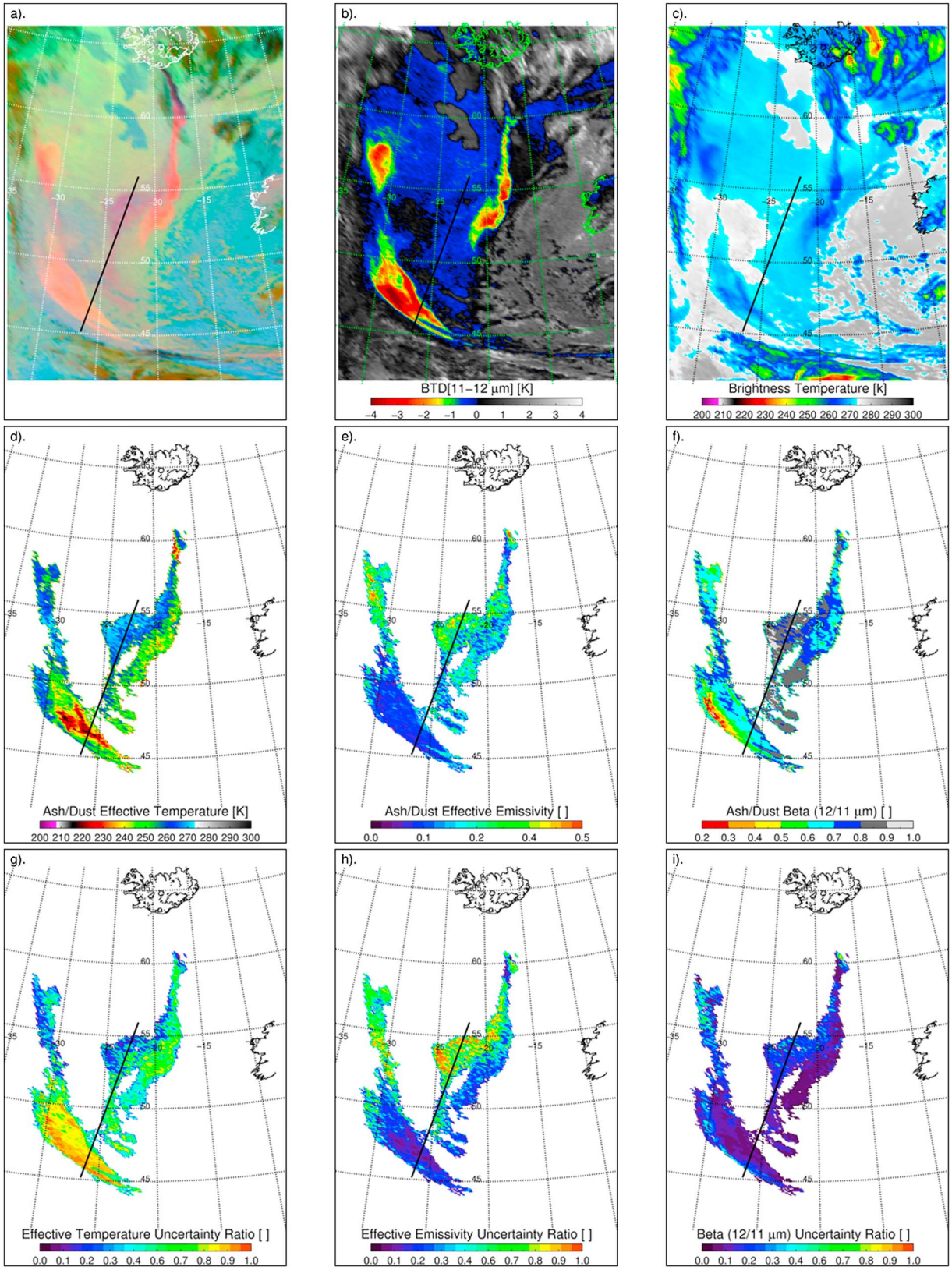

Figure 5. SEVIRI images from 0400 UTC on 8 May 2010 that show (a) dust RGB image, (b) "split-window" imagery, (c) 11 μm imagery, (d) retrieved effective cloud temperature, (e) retrieved effective cloud emissivity, (f) retrieved 12/11 μm effective optical depth ratio, (g) retrieved effective cloud temperature uncertainty ratio, (h) retrieved effective cloud emissivity uncertainty ratio, and (i) retrieved 12/11 μm effective optical depth ratio uncertainty ratio. The black solid line through the cloud represents a CALIPSO overpass. The andesite mineral composition was used to generate these results.

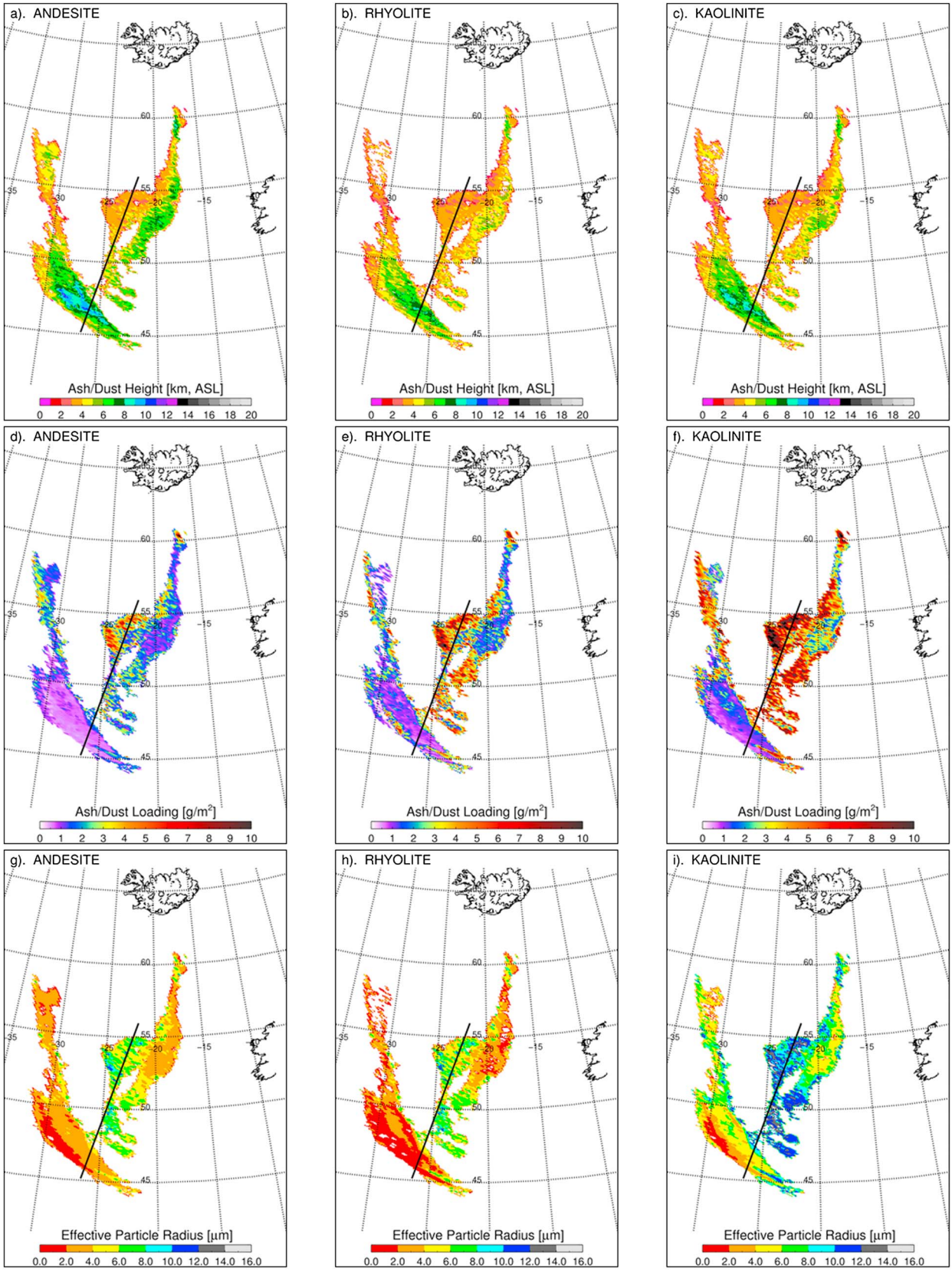

Figure 6. SEVIRI images from 0400 UTC on 8 May 2010 that show (a–c) retrieved effective cloud height as a function of mineral composition (andesite, rhyolite, and kaolinite, respectively), (d–f) retrieved cloud mass loading as a function of mineral composition (andesite, rhyolite, and kaolinite, respectively), and (g–i) retrieved cloud effective radius as a function of mineral composition (andesite, rhyolite, and kaolinite, respectively). The black solid line through the cloud represents a CALIPSO overpass.

8. Results and Error Analysis

8.1. Eyjafjallajökull—8 May 2010 (04:00 UTC)

[34] The 14 April to 21 May 2010 eruption of Eyjafjallajökull [*Gudmundsson et al.*, 2010] in southern Iceland had an extensive impact on aviation. Ash clouds from 2010 eruption of Eyjafjallajökull have been studied using ground [*Ansmann et al.*, 2010; *Arason et al.*, 2011; *Flentje et al.*, 2010; *Gasteiger et al.*, 2011], airborne [*Schumann et al.*, 2011; *Turnbull et al.*, 2012; *Newman et al.*, 2012; *Marenco et al.*, 2011; *Johnson et al.*, 2012], and satellite [*Winker et al.*, 2012; *Francis et al.*, 2012; *Stohl et al.*, 2011; *Newman et al.*, 2012; Prata and *Prata*, 2012] observations. In this study, the GOES-R retrieval results will primarily be compared to ash cloud properties inferred from the Cloud Aerosol Lidar with Orthogonal Polarization (CALIOP) [*Hunt et al.*, 2009] on board the Cloud Aerosol Lidar and Infrared Pathfinder Satellite Observation (CALIPSO) [*Winker et al.*, 2010] since those data provide detailed information on cloud vertical structure and are readily and freely available. In addition, unlike fixed location ground-based measurements and aircraft measurements, CALIOP samples ash and dust clouds globally over a large range of background conditions. Thus, just as described by *Heidinger and Pavolonis* [2009], the CALIOP data set is an ideal starting point for algorithm validation. Quantitative comparisons to aircraft observations will be performed in the future when those data sets are more readily available to the broader scientific community. Detailed comparisons to ground-based measurements and other published satellite retrieval data sets are beyond the scope of this paper (describe and justify our methodology) and will also be the focus of future research.

[35] Figures 5–7 show the results of the GOES-R ash cloud property retrieval on 8 May 2010 at 04:00 UTC. Satellite imagery and the core retrieval outputs, T_{eff} (K), $\varepsilon(11\,\mu\mathrm{m})$, $\beta(12/11\,\mu\mathrm{m})$, and associated uncertainties are shown in Figure 5. The andesite mineral composition was used to generate the results shown in Figure 5. Consistent with *Heidinger and Pavolonis* [2009], the uncertainties are expressed as the ratio of the estimated 1-σ-retrieval error and the a priori error estimate, where a value of 1.0 indicates that the uncertainties are identical and the retrieval added no

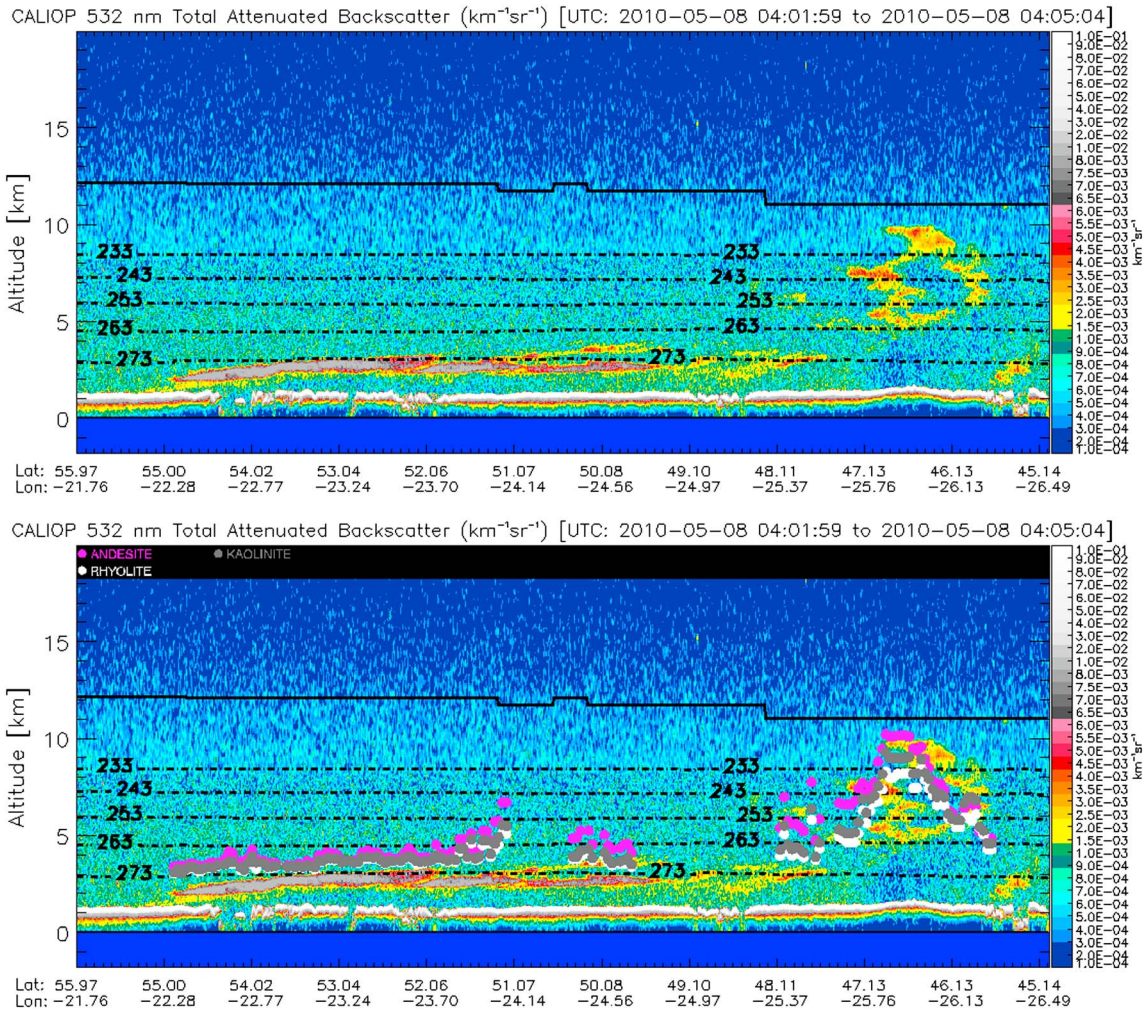

Figure 7. A CALIOP 532 nm total attenuated backscatter cross section from 04:01:59 UTC–04:05:04 UTC on 8 May 2012. The cross-section is shown with (bottom) and without (top) the retrieved SEVIRI cloud heights (as a function of the assumed mineral composition) overlaid. Magenta circles represent andesite. White circles denote rhyolite. Gray circles represent kaolinite. In both panels, the solid black line denotes the tropopause and the dashed black lines represent select atmospheric isotherms (in Kelvin).

value (ratios much less than 1.0 indicate that the retrieval added considerable value). Figure 6 shows the ash cloud height, mass loading, and effective particle radius, which were derived from T_{eff}, $\varepsilon(11\,\mu\mathrm{m})$, and $\beta(12/11\,\mu\mathrm{m})$ as described earlier. In order to help assess the sensitivity to mineral composition, the height (km above sea level), mass loading (g/m^2), and effective radius (μm) results are shown for three different mineral compositions, andesite (left column), rhyolite (middle column), and kaolinite (right column). Finally, Figure 7 shows the 532 nm total attenuated backscatter from a CALIOP cross-section through the ash cloud at 04:00 UTC. The ash cloud height results from each composition are overlaid on the cross section shown in the bottom panel of Figure 7. SEVIRI parallax effects were accounted for when co-locating SEVIRI and CALIOP and measurement times never differed by more than 7.5 min. For reference, the CALIPSO ground track is overlaid on each panel in Figures 5 and 6 (black line).

[36] Figures 5c and 5d show that T_{eff} is generally much less than the 11 μm brightness temperature and $\varepsilon(11\,\mu\mathrm{m})$ is generally less than 0.5, meaning the cloud is semi-transparent to infrared radiation and deviates strongly from blackbody behavior. This is true for nearly all ash/dust clouds analyzed in this paper. Also seen in Figures 5g–5i is the uncertainty ratio that for each of the retrieved parameters is generally <0.90, indicating that the retrieval is adding skill to the first guess. This scene is particularly interesting because the retrieval results indicate that there is considerable spatial variability in the ash cloud properties along the CALIPSO ground track, with higher heights (lower T_{eff}), lower loadings (smaller $\varepsilon(11\,\mu\mathrm{m})$ and $\beta(12/11\,\mu\mathrm{m})$), and smaller effective radii in the southwest portion of the ground track compared to the northeast portion. Figure 7 shows that the GOES-R retrievals are very consistent with the 1/3 km 532 nm CALIOP total attenuated backscatter profile which shows a more strongly attenuating lower level ash cloud in the northeast part of the overpass segment and much higher ash cloud layers with weaker attenuation in the southwest. The overall cloud height variation is captured by the GOES-R retrieval regardless of the assumed mineral composition. The retrieved mass loading and effective radius, however, are more sensitive to mineral composition, with kaolinite producing much larger (in some cases a factor of 2 larger) mass loadings and effective radii than andesite or rhyolite (see Figure 6). A more rigorous, quantitative, validation analysis will be shown later as a function of the mineral composition. One of the main limitations

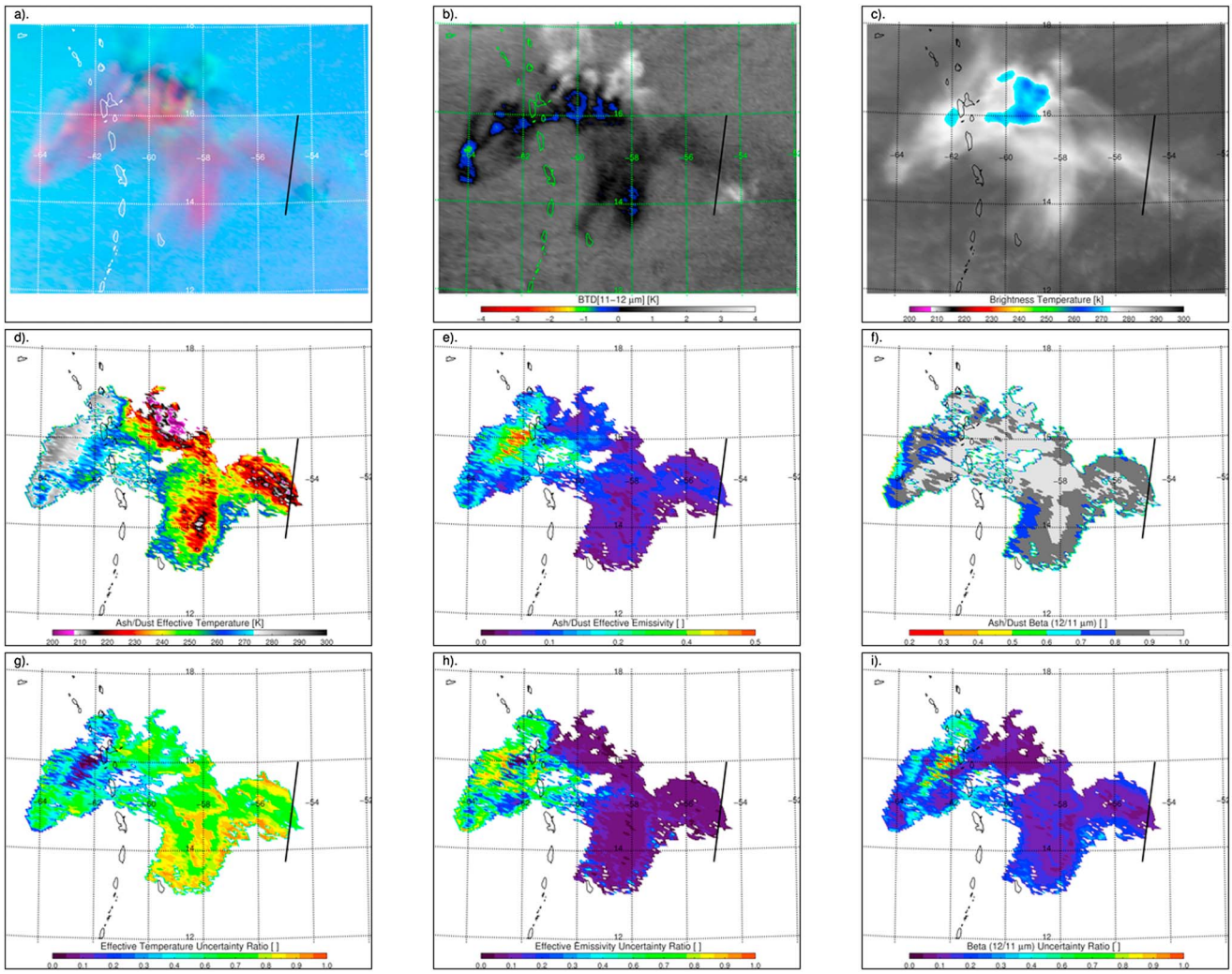

Figure 8. Same as Figure 5 except for the eastern Caribbean on 0530 UTC on 12 February 2010. The andesite mineral composition was used to generate these results.

of our methodology, and all previously published passive satellite sensor ash/dust retrieval algorithms, is that ash/dust cloud properties can only be retrieved if ash/dust is the highest cloud layer. In this scene the false color image (dust RGB) (Figure 5a) indicates that cirrus clouds overlap the ash cloud just south of Iceland. Thus, ash cloud properties could not be determined for this part of the ash cloud.

8.2. Soufriere Hills—12 February 2010 (05:30 UTC)

[37] Soufriere Hills is located in the eastern Caribbean, on the island of Montserrat. On 11 February 2010, a major partial lava dome collapse occurred, resulting in pyroclastic flows and a high-level ash cloud [Montserrat Volcano Observatory: http://www.mvo.ms]. Figures 8–10 show the results of the GOES-R ash cloud property retrieval on 12 February 2010 at 05:30 UTC in the same way as the Eyjafjallajökull example. The andesite mineral composition was assumed to generate the results shown in Figure 8. The meteorological background for this eruption is considerably different than that observed south of Iceland on 8 May 2010. A radiosonde from the nearby island of Guadeloupe indicated that the total precipitable water was 27.18 mm more than twice that observed at Keflavikur-Flugvollur in southern Iceland on 8 May 2010 (13.28 mm). As seen in Figure 8b, a significant portion of the ash cloud is characterized by a positive BTD(11–12 μm), consistent with a larger water vapor loading. Recall that the retrieval accounts for background variables, such as water vapor, so it should not be adversely impacted by positive values of BTD (11–12 μm). As in the Eyjafjallajökull example, T_{eff} is generally much less than the 11 μm brightness temperature and subsequently ε(11 μm) is also generally small, as is commonly the case with dispersed ash clouds (see Figures 8c and 8d). Most of the Soufriere Hills cloud is characterized by β(12/11 μm) values greater than 0.8. The uncertainty ratios indicate that the retrieval is adding considerable skill to the first guess for all retrieved parameters over most of the cloud. In the isolated patches where the T_{eff} uncertainty ratio is greater than 0.9, the ε(11 μm) and β(12/11 μm) uncertainty ratios are very small and vice versa, such that all three uncertainty ratios are never simultaneously large. There are a couple small holes in the cloud where conditions were such that ash was not detected using the procedure described earlier, and no retrieval was performed. Once again, the retrieved effective radius, and hence the mass loading, is far more sensitive to the assumed mineral composition than

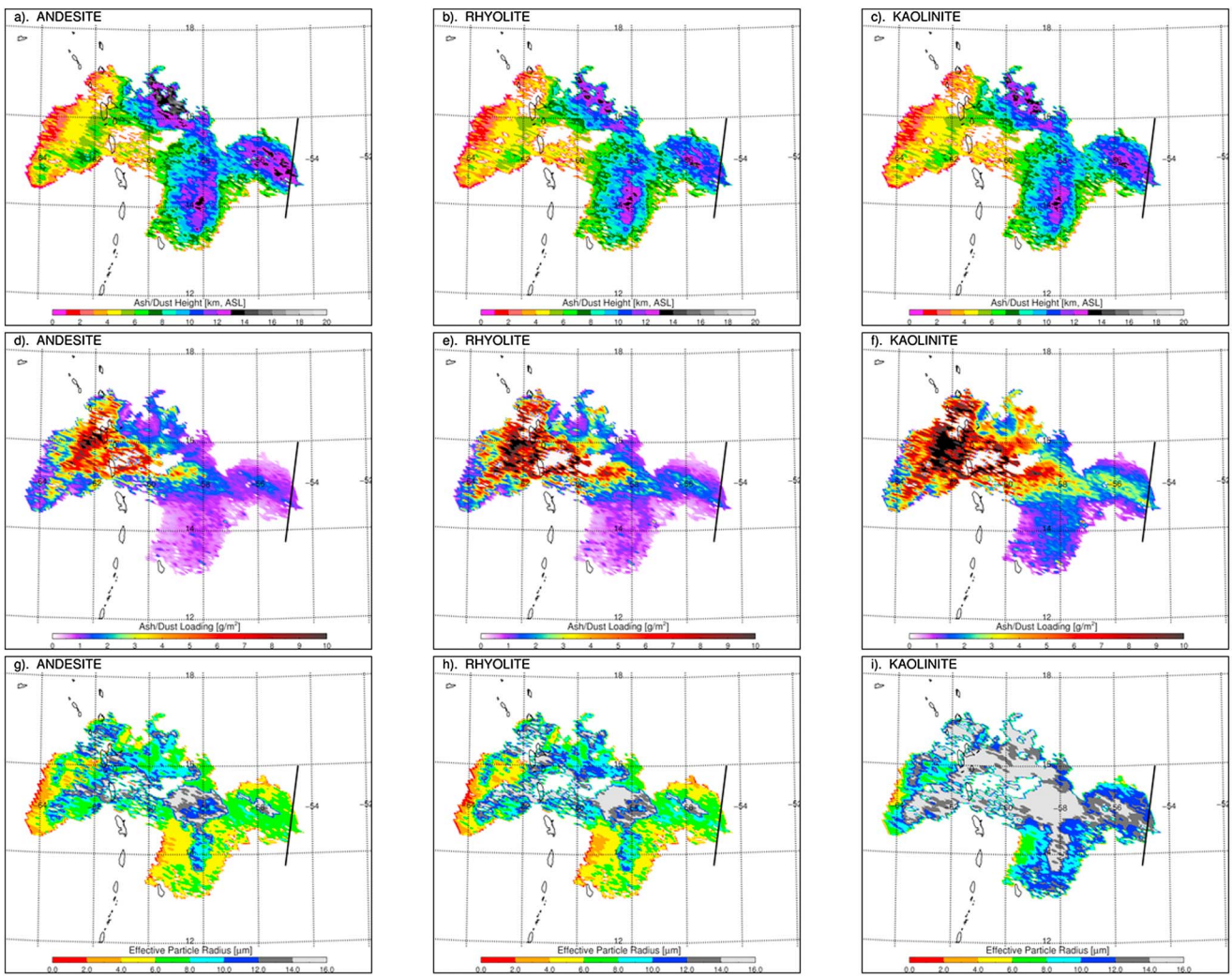

Figure 9. Same as Figure 6 except for the eastern Caribbean on 0530 UTC on 12 February 2010.

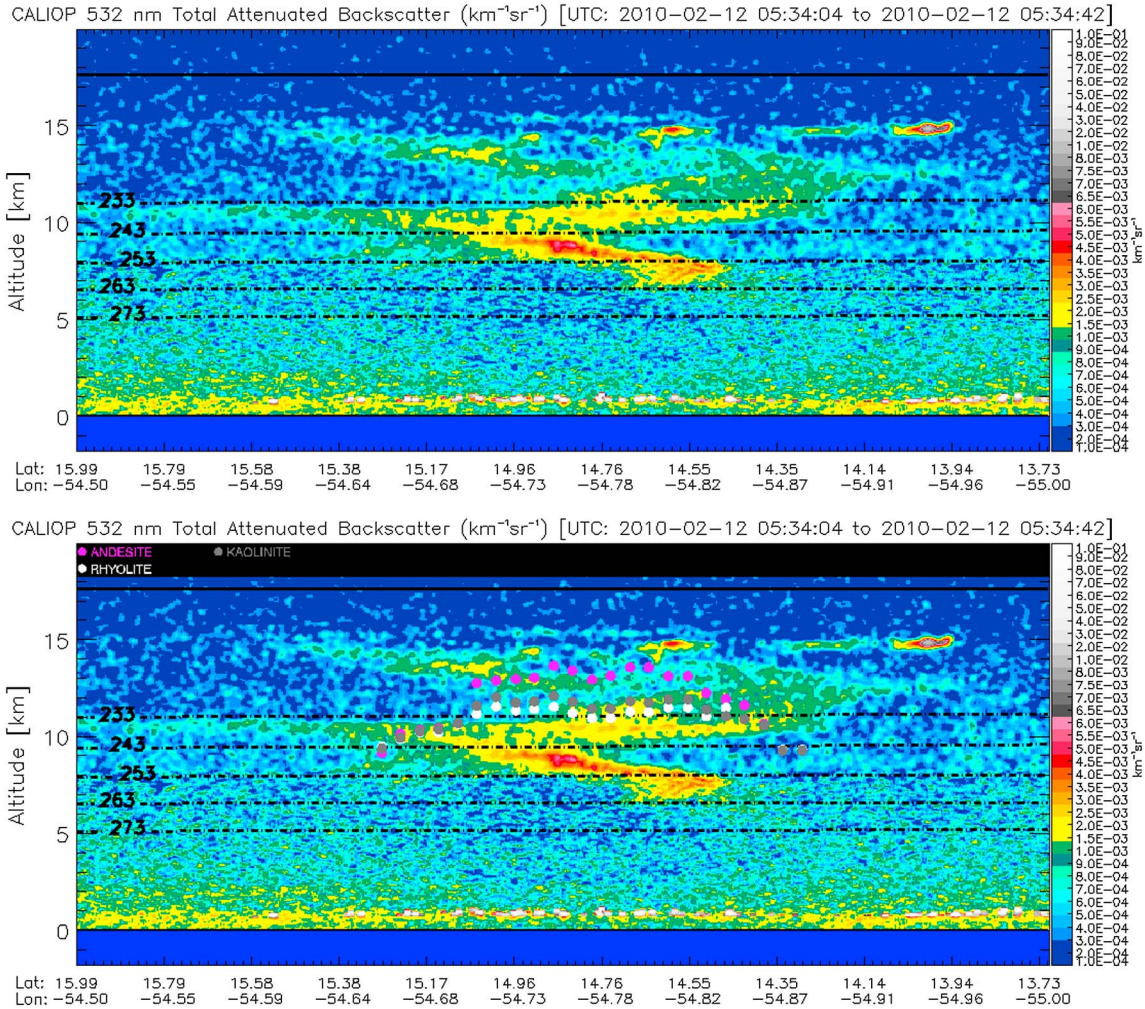

Figure 10. Same as Figure 7 except for 05:34:04 UTC–05:34:42 UTC on 12 February 2010.

the cloud height (see Figure 9). The retrieved cloud heights are also in good agreement with the CALIOP cross section (Figure 10) through the optically thin eastern portion of the cloud, with andesite producing a slightly better match than rhyolite and kaolinite. The low heights (<2 km) sometimes observed on the very edge of the Soufriere Hills cloud are likely caused by sub-pixel cloudiness (e.g., cloud fraction <1.0 within a given satellite pixel), which is not accounted for in the retrieval. Retrieval results and uncertainty estimates at the very edge of clouds should be used with caution, especially when the size of a satellite pixel is large, as it is in this case (SEVIRI pixels have a horizontal resolution of 10 km or greater in this region).

8.3. Saharan Dust—22 June 2007 (02:45 UTC)

[38] While the retrieval methodology described in this paper was developed, primarily, for volcanic ash cloud applications, it can also be used to estimate dust cloud properties. Figures 11–13 illustrate how the retrieval works on a Saharan dust cloud near the west coast of Africa, captured by SEVIRI on 22 June 2007 at 02:45 UTC. It should be noted that the horizontal resolution of the GFS model data used in this case study is 1° (0.5° data were used for the previous two cases), so the retrieved properties are slightly "blocky" as a result. As with the Eyjafjallajökull and Soufriere Hills volcanic ash clouds, the retrieved T_{eff} (Figure 11c) throughout the Saharan dust cloud is often much less than the 11 μm brightness temperature (Figure 11d) and ε(11 μm) rarely exceeds 0.3 (Figure 11e). The kaolinite mineral composition was used to generate the results shown in Figure 11. The T_{eff} uncertainty ratio often exceeds 0.9 (medium and dark orange colors in Figure 11g) when ε(11 μm) is smaller than about 0.05 (see Figure 11e), indicating that the retrieval of T_{eff} adds little to no value to the first guess for the most optically thin portions of this dust cloud. In contrast, the ε(11 μm) and β(12/11 μm) uncertainty ratios (Figures 11h and 11i, respectively) are nearly always less than 0.7, regardless of cloud opacity. The uncertainty ratio for all three retrieved parameters is generally greater over land than water because, as described earlier, the uncertainty in the modeled clear sky brightness temperatures is much greater over land than water. Figure 12 shows that the retrieval of cloud height, mass loading, and effective particle radius is quite sensitive to the mineral composition. In particular, using gypsum as the mineral composition results in lower cloud heights (higher T_{eff}), which must be radiatively compensated for by larger values of ε(11 μm) (not shown). The larger gypsum-derived mass loadings are caused by the larger values of ε(11 μm). This particular Saharan dust scene

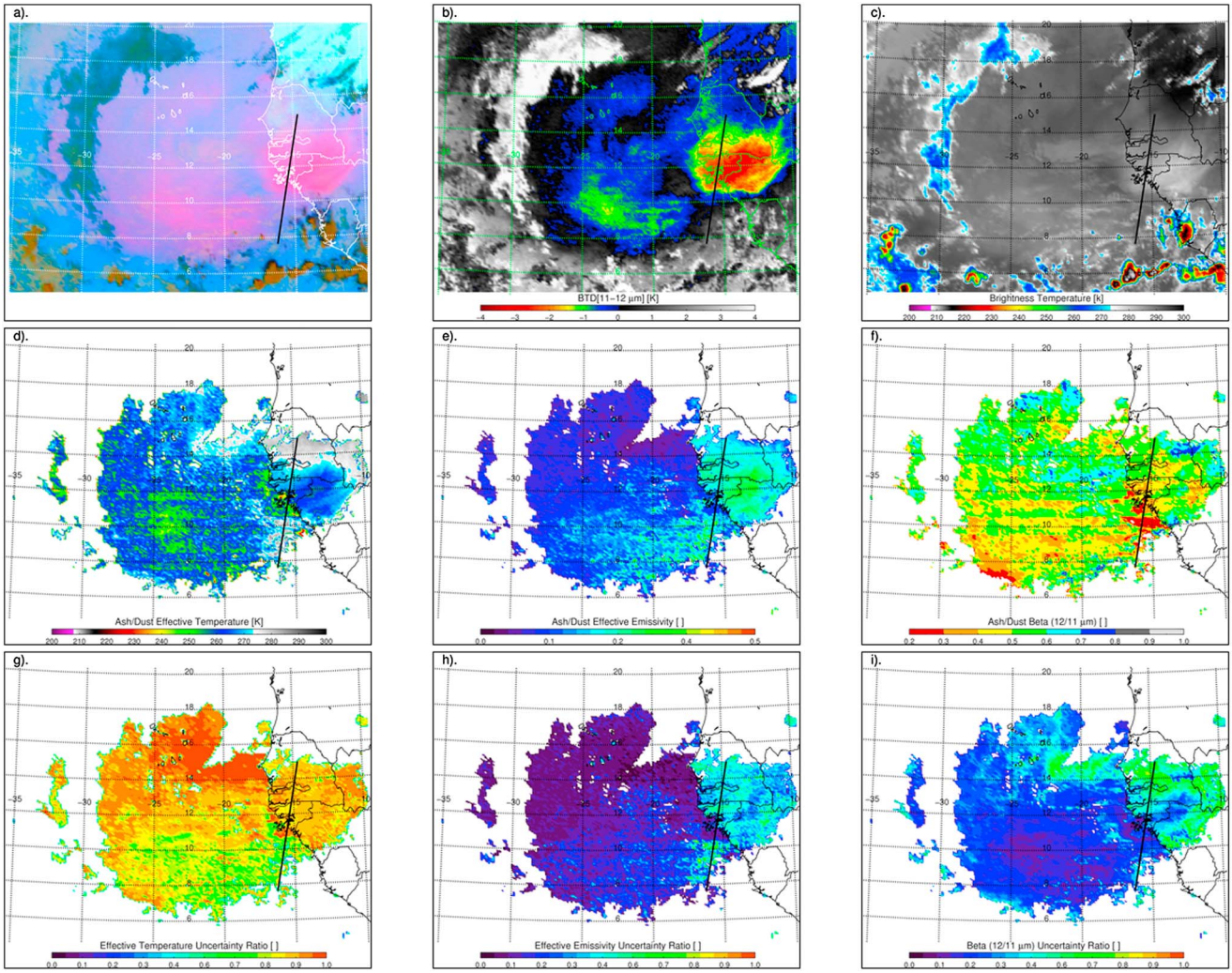

Figure 11. Same as Figure 5 except for a dust outbreak near the west coast of Africa on 0245 UTC on 22 June 2007. The kaolinite mineral composition was used to generate these results.

was chosen for analysis because the CALIPSO overpass includes observations over water and land (Figure 13). Figure 13 shows that the retrieved cloud heights tend to be overestimated near the coastline when using kaolinite or andesite. Coastlines are challenging in that surface temperature can vary greatly over relatively small distances. The spatial variability of surface temperature is not captured well by course resolution global models like the GFS (the horizontal resolution of the GFS data used for this scene is 1.0°). Thus, larger errors in the modeled clear sky brightness temperatures are likely. Over the land portion of this segment, the mineral composition has only a small impact on the retrieved height, consistent with a T_{eff} that does not deviate much from the first guess value. In fact, T_{eff} is generally within 5 K of the first guess along the land portion of the CALIOP cross-section. Over the water, using gypsum causes the cloud height to be underestimated more than kaolinite, perhaps suggesting that kaolinite is more likely to be the dominant mineral composition of this cloud. *Turner* [2008] found that the dominant mineral composition of Saharan dust clouds was kaolinite. Interestingly, even though this cloud is not composed of andesite, the cloud heights retrieved using the andesite composition are generally consistent with kaolinite. Using andesite, however, will cause the effective radius, and consequently the mass loading, to be underestimated relative to kaolinite. This case study does show that the general retrieval approach can be applied to dust clouds. Future work will focus on performing a more extensive dust cloud evaluation.

8.4. Statistical Comparison to CALIOP

[39] More rigorous comparisons to CALIOP-derived cloud properties are used to quantitatively assess the GOES-R retrieval algorithm. A total of 15 CALIPSO ash cloud overpasses from the 6–16 May portion of the 2010 Eyjafjallajökull eruption, and the CALIPSO overpass from the Soufriere Hills ash clouds shown in Figure 10 was manually chosen for this analysis. The only criterion used in the manual selection process was that ash had to be the highest cloud layer. When fully automated techniques have been developed to mine the CALIOP data record for ash clouds, this analysis can be readily expanded. Currently, confidently identifying ash clouds in CALIOP data is a manually intensive process that requires side-by-side close examination of CALIOP and multi-spectral infrared imagery, as ash clouds are very difficult to identify using CALIOP alone [*Winker et al.*, 2012]. The CALIPSO overpasses of Eyjafjallajökull

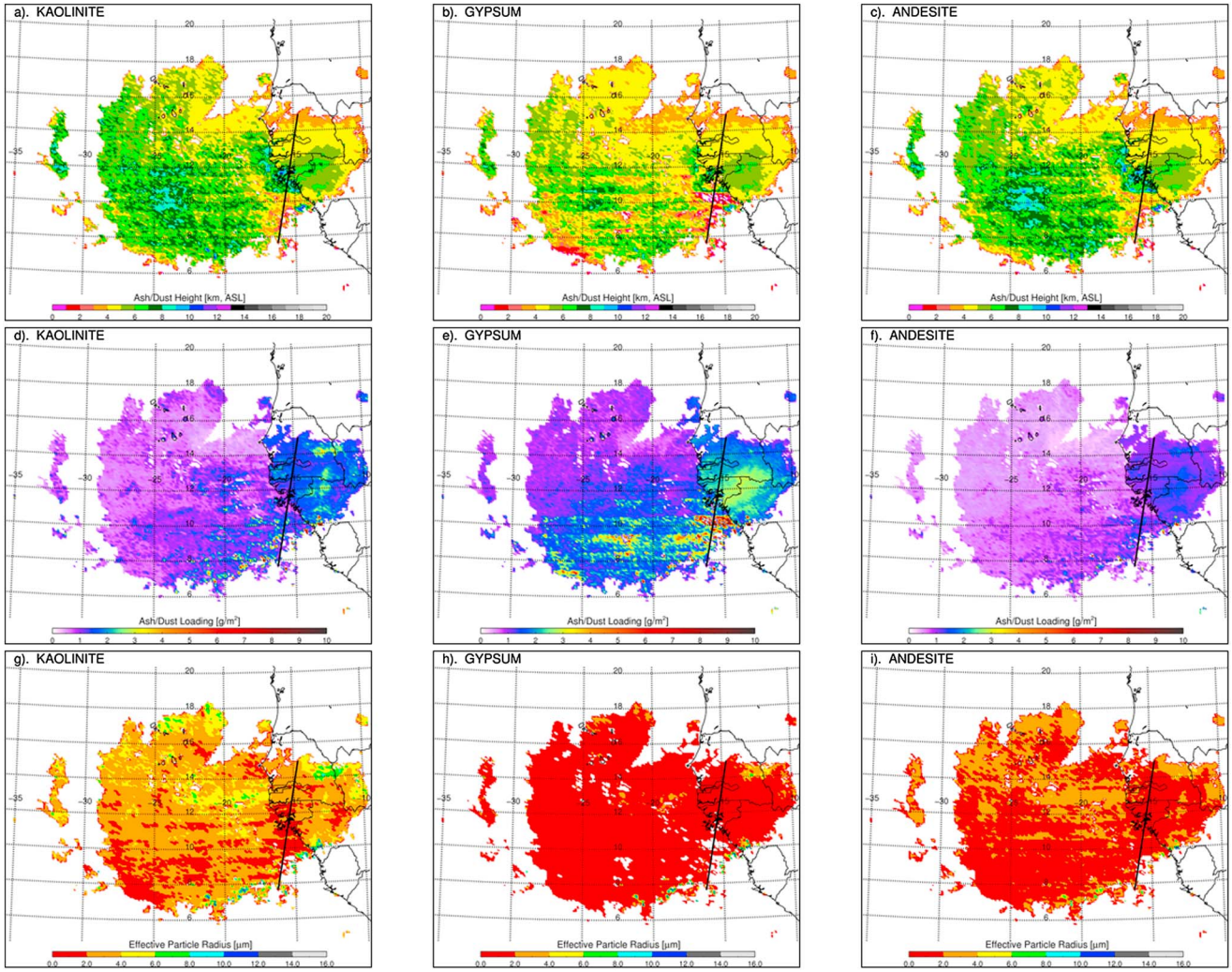

Figure 12. SEVIRI images near the west coast of Africa on 0245 UTC on 22 June 2007 that show (a–c) retrieved effective cloud height as a function of mineral composition (kaolinite, gypsum, and andesite, respectively), (d–f) retrieved cloud mass loading as a function of mineral composition (kaolinite, gypsum, and andesite, respectively), and (g–i) retrieved cloud effective radius as a function of mineral composition (kaolinite, gypsum, and andesite, respectively). The black solid line through the cloud represents a CALIPSO overpass.

ash clouds are conveniently well known due to the high impact of that eruption on air traffic, which is not the case with many other eruptions sampled by CALIOP. The 16 ash cloud overpasses result in a total of 796 data points, which is large relative to previously published quantitative, ash cloud validation efforts [e.g., *Francis et al.*, 2012; Prata and *Prata*, 2012].

[40] A combination of the 5 km CALIOP cloud and aerosol cloud layers products [*Vaughan et al.*, 2009] is used to determine the vertical extent of the highest cloud layer along each segment through the ash clouds. A combination of the cloud and aerosol layers products is needed since some ash clouds will be classified as aerosol and some will be classified as clouds (liquid or ice) by the classification algorithm [e.g. *Winker et al.*, 2012]. In addition, effective cloud emissivity for a given SEVIRI spectral band or bands can be computed using a combination of CALIOP vertical cloud boundaries and co-located SEVIRI infrared measurements [e.g., *Heidinger and Pavolonis*, 2009; *Garnier et al.*, 2012]. We utilize the method of *Heidinger and Pavolonis*, 2009 to compute the $\varepsilon(11\,\mu m)$, and $\beta(12/11\,\mu m)$ of the highest cloud layer. The $\varepsilon(11\,\mu m)$ and $\beta(12/11\,\mu m)$ computed from a combination of CALIOP and SEVIRI will be consistently more accurate than the $\varepsilon(11\,\mu m)$ and $\beta(12/11\,\mu m)$ retrieved using SEVIRI alone (with the GOES-R retrieval approach) because CALIOP vertical cloud boundaries provide a very tight constraint on T_{eff} and no cloud microphysical assumptions are needed (see equations (1) and (2)). In the GOES-R retrieval, T_{eff} is a very loosely constrained free parameter and cloud microphysical assumptions related to particle composition, shape, and size are needed (e.g., Figure 1). Because no microphysical assumptions are needed to determine cloud top height, $\varepsilon(11\,\mu m)$, and $\beta(12/11\,\mu m)$ from CALIOP or a combination of CALIOP and SEVIRI (in the case of $\varepsilon(11\,\mu m)$ and $\beta(12/11\,\mu m)$), we focus on validating these parameters. Mass loading and effective particle radius are not quantitatively evaluated since these cannot be determined from CALIOP without making assumptions about

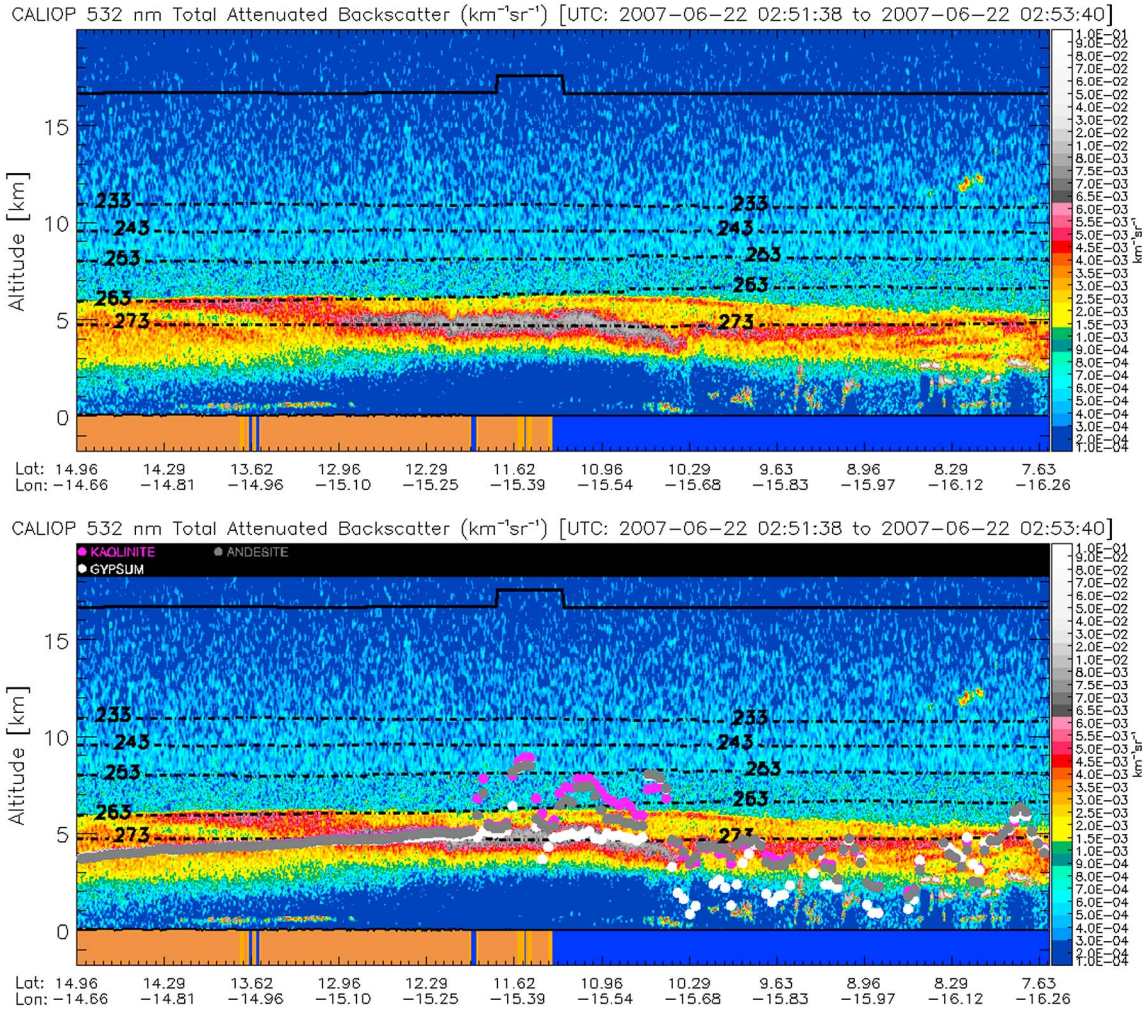

Figure 13. Same as Figure 7 except for 02:51:38 UTC–02:53:40 UTC on 22 June 2007. Unlike Figure 7, magenta circles represent kaolinite, white circles denote gypsum, and gray circles represent andesite.

particle composition, size, and shape. However, the evaluation of $\varepsilon(11\,\mu m)$, and $\beta(12/11\,\mu m)$ will provide valuable insight into the parameters needed to determine the mass loading and effective radius. In the future, we will utilize any aircraft- and ground-based measurements that are available to evaluate the mass loading and effective radius, although microphysical assumptions still need to be made.

[41] A comparison between the GOES-R ash cloud heights and the CALIOP cloud top heights is shown in Figure 14 as a function of the $\varepsilon(11\,\mu m)$ computed from a combination of CALIOP and SEVIRI, the cloud geometrical thickness provided by CALIOP, and the mineral composition (andesite, rhyolite, or kaolinite) used in the GOES-R retrieval. The cloud heights retrieved using the GOES-R approach are generally in good agreement with CALIOP, regardless of the mineral composition used in the retrieval (although andesite seems to have a slight edge). The GOES-R heights are negatively biased (-0.77 km for andesite) relative to the CALIOP cloud top, which is expected given the high vertical resolution of CALIOP and the coarse vertical resolution of SEVIRI (the measured radiation originates from a thicker layer within the cloud). Not surprisingly, the most optically thin clouds ($\varepsilon(11\,\mu m) < 0.05$) are responsible for most of the low bias. Clouds with a larger geometric thickness are also more prone to underestimation since the measured infrared radiation is now emanating from a thicker layer below the cloud top. The GOES-R approach sometimes slightly overestimates the cloud top height, especially for ash clouds with tops lower than 5 km. The overestimation can generally be attributed to underlying stratus clouds that are colder than the surface. Underlying cloud layers are not accounted for in the retrieval at this time, but future versions of the retrieval will account for underlying clouds.

[42] Figure 15 shows a comparison between $\varepsilon(11\,\mu m)$ retrieved using the GOES-R algorithm and $\varepsilon(11\,\mu m)$ computed from a combination of CALIOP and SEVIRI. The results are shown as a function of the CALIOP cloud top height, CALIOP geometric cloud thickness, and the mineral composition (andesite, rhyolite, or kaolinite) used to perform the GOES-R retrieval. The GOES-R bias in $\varepsilon(11\,\mu m)$ is very small, especially when the retrieval is performed using andesite (bias = -0.006). The standard deviation (or precision) of the GOES-R – CALIOP difference is considerably larger because a positive bias is observed when the CALIOP derived $\varepsilon(11\,\mu m) < 0.3$ and a negative bias is observed when $\varepsilon(11\,\mu m) > 0.3$. Closer inspection of the CALIOP cross sections used in this analysis reveals that the positive bias at smaller emissivity values is likely a result of the presence

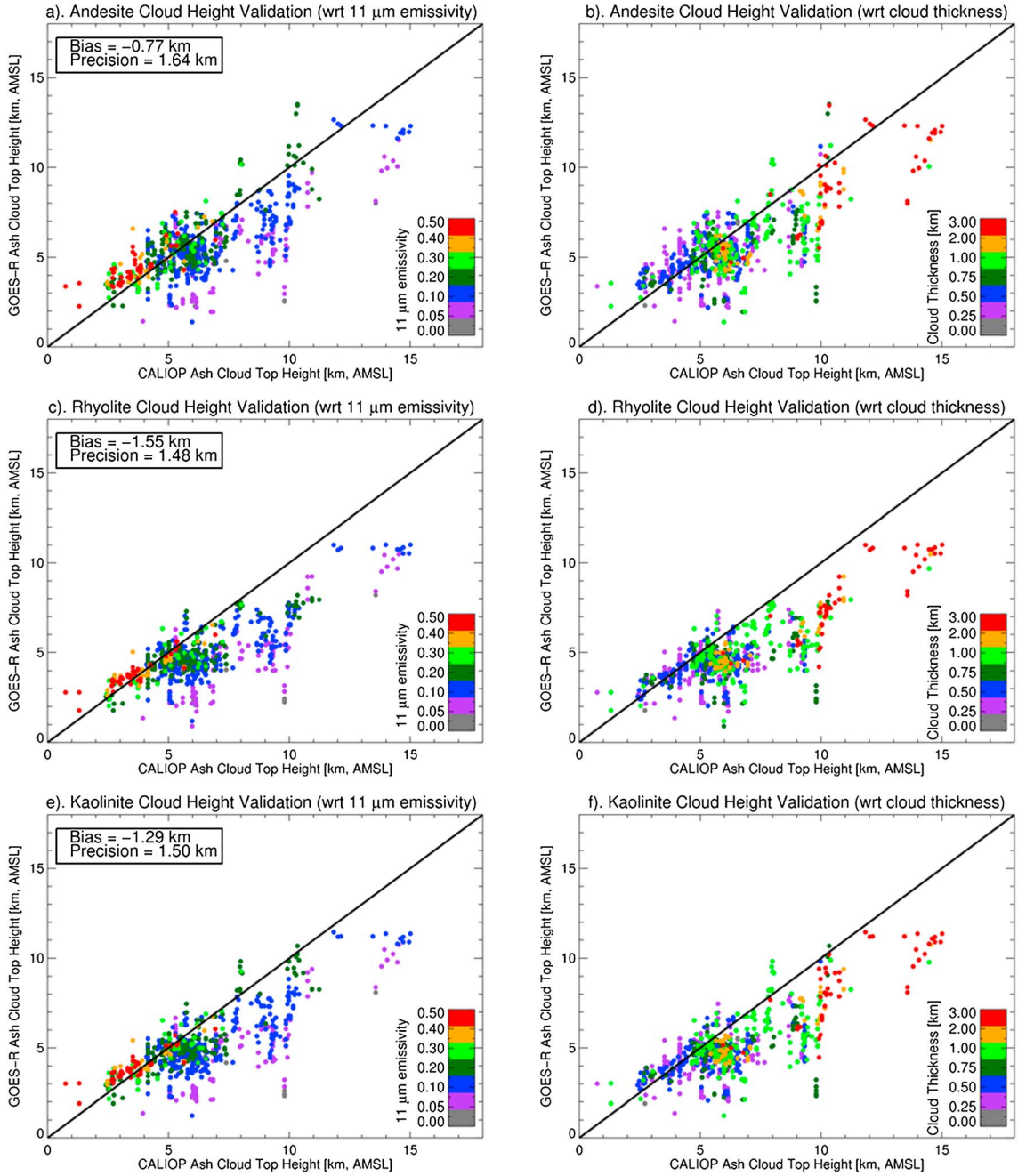

Figure 14. A comparison of SEVIRI ash cloud heights retrieved using the GOES-R approach and CALIOP measured cloud top heights is shown as a function of the nadir 11 μm cloud emissivity derived from a combination of CALIOP and SEVIRI (first column) and the cloud geometric thickness given by CALIOP (second column). Each color represents a different 11 μm cloud emissivity or cloud thickness bin. The results are also shown as a function of the mineral composition (andesite (top), rhyolite (middle), and kaolinite (bottom)) assumed by the retrieval. The 1 : 1 line is shown in black. A total of 796 data points were used in this analysis.

of multiple, geometrically thin, ash cloud layers with very little vertical separation. While underlying cloud layers are accounted for in the computation of the combined CALIOP/SEVIRI 11 μm cloud emissivity, they are not accounted for in the GOES-R retrieval. Conversely, the negative bias observed at larger emissivity values is caused by the underestimation of T_{eff} (overestimation of cloud height) discussed earlier.

[43] Finally, a comparison between the GOES-R β(12/11 μm) and the β(12/11 μm) computed using a combination of CALIOP and SEVIRI is shown in Figure 16 as a function of the CALIOP cloud top height, the ε(11 μm) computed from a combination of CALIOP and SEVIRI measurements, and mineral composition. With the exception of a few outliers (mainly low to midlevel ash clouds), the β(12/11 μm) retrieved using the GOES-R algorithm is in very close agreement with the CALIOP β(12/11 μm), regardless of the mineral composition used in the retrieval (bias = 0.002 for andesite). Since the effective particle radius is determined directly from

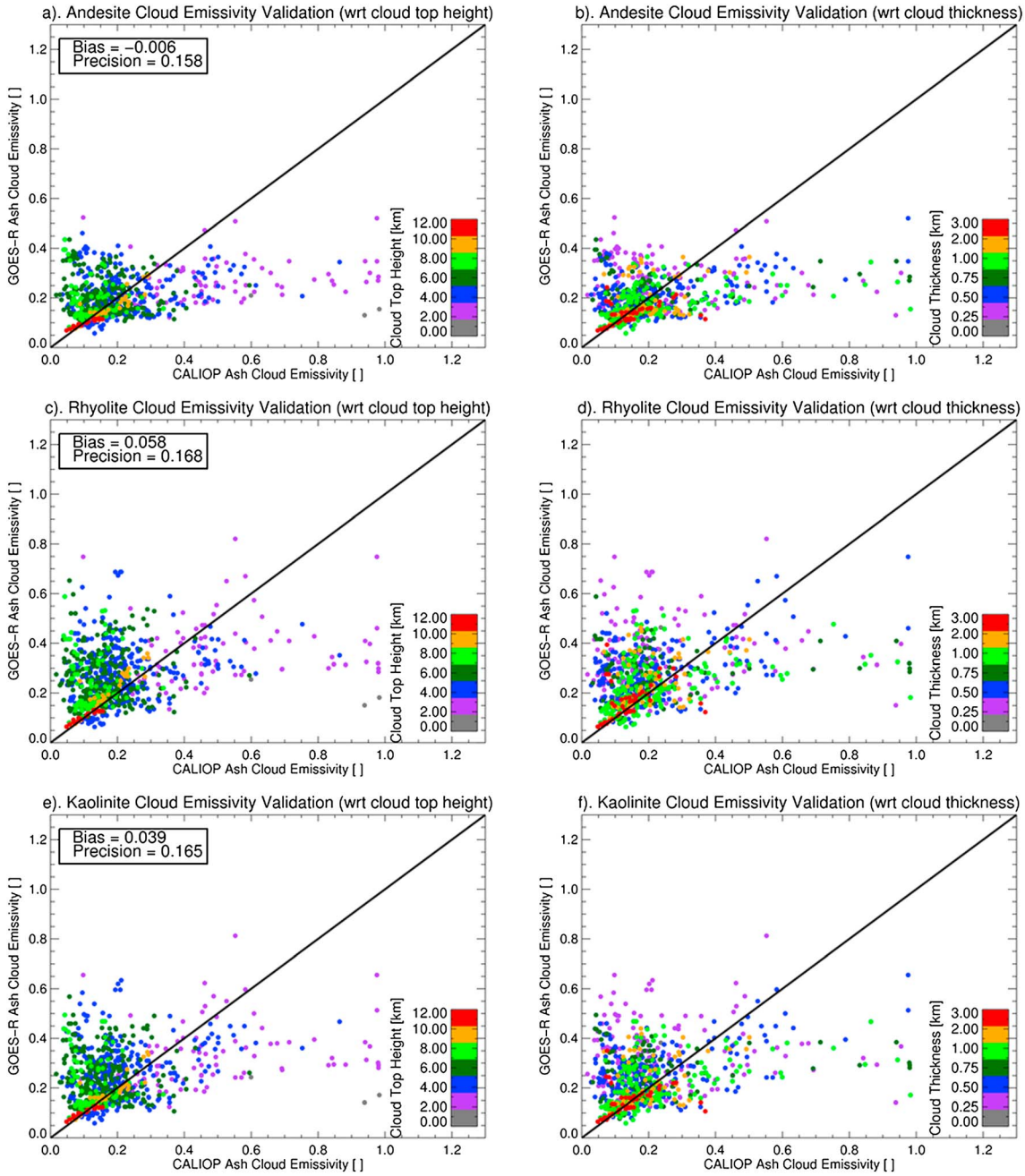

Figure 15. A comparison of SEVIRI ash cloud emissivity retrieved using the GOES-R approach and the 11 μm cloud emissivity derived from a combination of CALIOP and SEVIRI is shown as a function of the CALIOP-measured cloud top height (first column) and the cloud geometric thickness given by CALIOP (second column). Each color represents a different cloud top height or cloud thickness bin. The results are also shown as a function of the mineral composition (andesite (top), rhyolite (middle), and kaolinite (bottom)) assumed by the retrieval. The 1 : 1 line is shown in black. A total of 796 data points were used in this analysis.

β(12/11 μm) (see Figure 2), these results imply that the effective particle radius can be computed with a similarly small bias for a given known mineral composition. Given that β(12/11 μm) (and hence the effective particle radius) is largely unbiased, the bias in mass loading will primarily be a result of the bias in ε(11 μm), which is heavily influenced by underlying cloud layers. Thus, the mass loading of an ash cloud (with a known mineral composition and particle density) that overlays another cloud layer or layers will be positively biased when $\varepsilon(11\,\mu m) < 0.3$ and negatively biased when $\varepsilon(11\,\mu m) > 0.3$. Accounting for underlying cloud layers, even crudely, should help reduce the overall bias.

9. Conclusions and Future Work

[44] We have developed a fully automated algorithm to retrieve the cloud radiative temperature, emissivity, and a microphysical parameter of volcanic ash and dust clouds

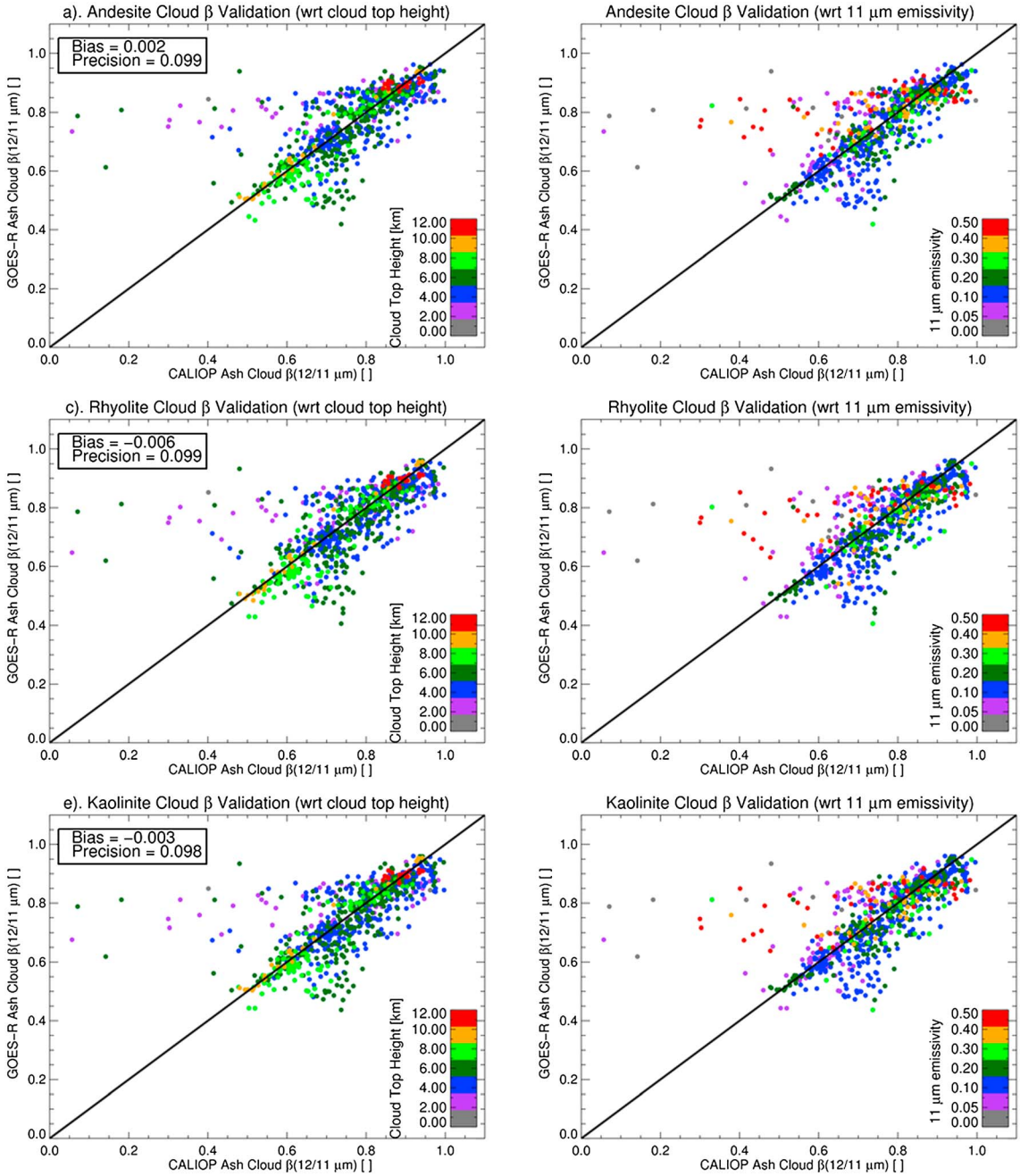

Figure 16. A comparison of SEVIRI ash 12/11 μm β-ratios retrieved using the GOES-R approach and the 12/11 μm β-ratios computed using a combination of CALIOP and SEVIRI is shown as a function of the cloud top height measured by CALIOP (first column) and the nadir 11 μm cloud emissivity derived from a combination of CALIOP and SEVIRI (second column). Each color represents a different cloud top height or 11 μm cloud emissivity bin. The results are also shown as a function of the mineral composition (andesite (top), rhyolite (middle), and kaolinite (bottom)) assumed by the retrieval. The 1 : 1 line is shown in black. A total of 796 data points were used in this analysis.

using satellite-based infrared measurements. From these retrieved parameters, the cloud radiative height, effective particle radius, optical depth, and mass loading can be derived, subject to certain assumptions. An optimal estimation framework is utilized, which allows uncertainties in the measurements and forward model to be taken into account and uncertainty estimates for each of the retrieved parameters to be determined. Background atmospheric water vapor, surface temperature, and surface emissivity are explicitly accounted for on a pixel-by-pixel basis, so the algorithm is globally applicable. The retrieval software has been demonstrated in real time and will provide the official operational volcanic ash products for GOES-R [*Pavolonis and Sieglaff*, 2010].

[45] Using SEVIRI as a proxy for the GOES-R ABI, the retrieval algorithm was applied to ash clouds from the 2010 eruption of Eyjafjallajökull, the 2010 eruption of Soufriere Hills, and a Saharan dust cloud. In an effort to

determine the accuracy of the retrieval, the results were compared to CALIOP-derived cloud properties. The GOES-R cloud heights were found to generally be within 1–2 km (with little bias) of CALIOP-derived cloud top heights for low and mid level ash clouds (<7 km) and within 3–4 km (with a negative bias) for high level clouds (>7 km). These results are consistent with the work of *Francis et al.* [2012]. The 11 μm cloud emissivity had a tendency to be positively biased relative to the cloud emissivity computed using CALIOP for clouds with a small 11 μm optical depth (<0.3) and negatively biased for clouds with an intermediate to large optical depth (>0.3), although nearly all clouds analyzed were semi-transparent to infrared radiation. The bias in the retrieved cloud emissivity is likely caused by complexities related to underlying cloud layers. Future versions of the retrieval will account for underlying cloud layers. The 12/11 μm optical depth ratio (β(12/11 μm)), which is directly related to the effective particle radius, closely agreed with the β(12/11 μm) computed using CALIOP, and was found to be unbiased. Consequently, the effective particle radius should also be largely unbiased. While mass loading was not quantitatively evaluated (it cannot be evaluated without making several assumptions), we can conclude that it will generally be biased in a similar manner as the cloud emissivity since β(12/11 μm) was shown to be accurate and unbiased. Much more work is needed to determine if the mass loading information can be used to quantitatively assess where damaging aircraft encounters are most likely to occur. In addition, better overall agreement between the retrieved and CALIOP-derived cloud properties was found when the andesite mineral composition was used to represent ash clouds and kaolinite was used to represent dust clouds. Future work will be aimed at determining if the selection of the mineral composition(s) can be performed in a more sophisticated manner.

[46] While the retrieval described in this paper was designed to use channels approximately centered at 11, 12, and 13.3 μm, the general retrieval framework can be applied to other channel combinations. For instance a water vapor absorption band (e.g., 6.7 μm) can be substituted for the 12 μm or 13.3 μm channels so that ash and dust cloud properties can be retrieved using a greater number of satellite sensors. Measurements from different sensors can also be combined to allow the retrieval to be performed using high spatial resolution sensors that lack a 13.3 μm band by approximating a 13.3 μm band from low spatial resolution hyperspectral infrared sounding instruments located on the same spacecraft (e.g., Advanced Very High Resolution Radiometer (AVHRR) + Infrared Atmospheric Sounding Interferometer (IASI); Visible Infrared Radiometer Suite (VIIRS) + Cross-Track Infrared Sounder (CrIS); and MODerate Resolution Imaging Spectroradiometer (MODIS) + Atmospheric Infrared Sounder (AIRS)). Hyperspectral instruments can also potentially be used to provide a better first guess for the retrieval, which will be the focus of future work.

[47] As recent case studies [*Stohl et al.*, 2011; *Schmehl et al.*, 2012; *Denlinger et al.*, 2012; *Webley et al.*, 2012] have shown, the ash/dust cloud property retrievals, like those presented here, can be used to initialize (improve the volcano source term, data assimilation applications, initialize trajectories, etc.) and validate dispersion and transport models. Current research is focused on developing a globally robust, fully automated, ash/dust detection method to facilitate using satellite retrievals of ash and dust cloud properties to improve operational modeling capabilities.

Appendix A

[48] Given our choice of forward model, an analytical expression for each element of the kernel matrix, **K**, can be derived from equations (1)–(3), (6)–(10), and the Planck function. The derivative of each of the forward model simulated observations with respect to T_{eff} is given by the following set of equations. In these equations, $\partial B(\lambda)/\partial T_{\mathrm{eff}}$ is the derivative of the Planck function with respect to the effective cloud temperature, T_{eff}, and $\partial B(\lambda)/\partial T$ is the derivative of the Planck function with respect to the forward model derived-brightness temperature. All other symbols have been previously defined.

$$\frac{\partial BT(11\,\mu\mathrm{m})}{\partial T_{\mathrm{eff}}} = \varepsilon(11\,\mu\mathrm{m})t_{\mathrm{ac}}(11\,\mu\mathrm{m})\left(\frac{\partial B(11\,\mu\mathrm{m})}{\partial T_{\mathrm{eff}}}\right)\left(\frac{\partial B(11\,\mu\mathrm{m})}{\partial T}\right)^{-1} \tag{A1}$$

$$\begin{aligned}\frac{\partial BTD(11-12\,\mu\mathrm{m})}{\partial T_{\mathrm{eff}}} = {} & \frac{\partial BT(11\,\mu\mathrm{m})}{\partial T_{\mathrm{eff}}} \\ & -\varepsilon(12\,\mu\mathrm{m})t_{\mathrm{ac}}(12\,\mu\mathrm{m})\left(\frac{\partial B(12\,\mu\mathrm{m})}{\partial T_{\mathrm{eff}}}\right) \\ & \times\left(\frac{\partial B(12\,\mu\mathrm{m})}{\partial T}\right)^{-1}\end{aligned} \tag{A2}$$

$$\begin{aligned}\frac{\partial BTD(11-13.3\,\mu\mathrm{m})}{\partial T_{\mathrm{eff}}} = {} & \frac{\partial BT(11\,\mu\mathrm{m})}{\partial T_{\mathrm{eff}}} \\ & -\varepsilon(13.3\,\mu\mathrm{m})t_{\mathrm{ac}}(13.3\,\mu\mathrm{m})\left(\frac{\partial B(13.3\,\mu\mathrm{m})}{\partial T_{\mathrm{eff}}}\right) \\ & \times\left(\frac{\partial B(13.3\,\mu\mathrm{m})}{\partial T}\right)^{-1}\end{aligned} \tag{A3}$$

[49] The following equations give the derivative of each forward model simulation with respect to ε(11 μm):

$$\frac{\partial BT(11\,\mu\mathrm{m})}{\partial \varepsilon(11\,\mu\mathrm{m})} = [R_{\mathrm{cld}}(11\,\mu\mathrm{m}) - R_{\mathrm{clr}}(11\,\mu\mathrm{m})]\left(\frac{\partial B(11\,\mu\mathrm{m})}{\partial T}\right)^{-1} \tag{A4}$$

$$\begin{aligned}\frac{\partial BTD(11-12\,\mu\mathrm{m})}{\partial \varepsilon(11\,\mu\mathrm{m})} = {} & \frac{\partial BT(11\,\mu\mathrm{m})}{\partial \varepsilon(11\,\mu\mathrm{m})} \\ & -[R_{\mathrm{cld}}(12\,\mu\mathrm{m}) - R_{\mathrm{clr}}(12\,\mu\mathrm{m})] \\ & \left[\beta(12/11\,\mu\mathrm{m})(1-\varepsilon(11\,\mu\mathrm{m}))^{\beta(12/11\mu\mathrm{m})-1}\right] \\ & \left(\frac{\partial B(12\,\mu\mathrm{m})}{\partial T}\right)^{-1}\end{aligned} \tag{A5}$$

$$\begin{aligned}\frac{\partial BTD(11-13.3\,\mu\mathrm{m})}{\partial \varepsilon(11\,\mu\mathrm{m})} = {} & \frac{\partial BT(11\,\mu\mathrm{m})}{\partial \varepsilon(11\,\mu\mathrm{m})} \\ & -[R_{\mathrm{cld}}(13.3\,\mu\mathrm{m}) - R_{\mathrm{clr}}(13.3\,\mu\mathrm{m})] \\ & \left[\beta(13.3/11\,\mu\mathrm{m})(1-\varepsilon(11\,\mu\mathrm{m}))^{\beta(13.3/11\mu\mathrm{m})-1}\right] \\ & \left(\frac{\partial B(13.3\,\mu\mathrm{m})}{\partial T}\right)^{-1}\end{aligned} \tag{A6}$$

[50] Finally, the derivative of each forward model simulation with respect to β(12/11 μm) is given by the following

equations. In equation (A9), $\partial\beta(13.3/11\,\mu m)/\partial\beta(12/11\mu m)$ is applied to equation (11).

$$\frac{\partial BT(11\,\mu m)}{\partial\beta(12/11\,\mu m)} = 0.0 \tag{A7}$$

$$\frac{\partial BTD(11-12\,\mu m)}{\partial\beta(12/11\,\mu m)} = [R_{cld}(12\,\mu m) - R_{clr}(12\,\mu m)] \ln[1-\varepsilon(11\,\mu m)][1-\varepsilon(12\,\mu m)]\left(\frac{\partial B(12\,\mu m)}{\partial T}\right)^{-1} \tag{A8}$$

$$\frac{\partial BTD(11-13.3\,\mu m)}{\partial\beta(12/11\,\mu m)} = [R_{cld}(13.3\mu m) - R_{clr}(13.3\mu m)] \ln[1-\varepsilon(11\mu m)][1-\varepsilon(13.3\mu m)] \left(\frac{\partial\beta(13.3/11\mu m)}{\partial\beta(12/11\mu m)}\right)\left(\frac{\partial B(13.3\mu m)}{\partial T}\right)^{-1} \tag{A9}$$

[51] **Acknowledgments.** The CALIOP data were obtained from the NASA Langley Research Center Atmospheric Science Data Center. We thank the three anonymous reviewers for their helpful suggestions and comments. The views, opinions, and findings contained in this report are those of the author(s) and should not be construed as an official National Oceanic and Atmospheric Administration or U.S. Government position, policy, or decision.

References

Ansmann, A., et al. (2010), The 16 April 2010 major volcanic ash plume over central Europe: EARLINET lidar and AERONET photometer observations at Leipzig and Munich, Germany, *Geophys. Res. Lett.*, *37*, doi:10.1029/2010GL043809 ER.

Arason, P., G. N. Petersen, and H. Bjornsson (2011), Observations of the altitude of the volcanic plume during the eruption of Eyjafjallajokull, April–May 2010, *Earth Syst. Sci. Data*, *3*, 9–17, doi:10.5194/ESSD-3-9-2011.

Casadevall, T. (1994), The 1989–1990 eruption of Redoubt Volcano, Alaska—Impacts on aircraft operations, *J. Volcanol. Geotherm. Res.*, *62*, 301–316, doi:10.1016/0377-0273(94)90038-8.

Clarisse, L., D. Hurtmans, A. J. Prata, F. Karagulian, C. Clerbaux, M. De Maziere, and P. Coheur (2010), Retrieving radius, concentration, optical depth, and mass of different types of aerosols from high-resolution infrared nadir spectra, *Appl. Opt.*, *49*, 3713-3722.

Corradini, S., C. Spinetti, E. Carboni, C. Tirelli, M. F. Buongiorno, S. Pugnaghi, and G. Gangale (2008), Mt. Etna tropospheric ash retrieval and sensitivity analysis using Moderate Resolution Imaging Spectroradiometer measurements, *J Appl Remote Sens*, *2*, doi:10.1117/1.3046674 ER.

Cox, S. K. (1976), Observations of cloud infrared effective emissivity, *J. Atmos. Sci.*, *33*, 287–289.

Denlinger, R. P., M. Pavolonis, and J. Sieglaff (2012), A robust method to forecast volcanic ash clouds, *J Geophys Res-Atmos*, *117*, D13208, doi:10.1029/2012JD017732.

DeSouza-Machado, S. G., et al. (2010), Infrared retrievals of dust using AIRS: Comparisons of optical depths and heights derived for a North African dust storm to other collocated EOS A-Train and surface observations, *J Geophys Res Atmos*, *115*, D15201, doi:10.1029/2009JD012842.

Dunion, J. P., C. S. Velden (2004), The impact of the Saharan air layer on Atlantic tropical cyclone activity, *Bull. Am. Meteorol. Soc.*, *85*, 353–365, doi:10.1175/BAMS-85-3-353-365 ER.

Evan, A. T., D. J. Vimont, A. K. Heidinger, J. P. Kossin, and R. Bennartz (2009), the role of aerosols in the evolution of tropical North Atlantic Ocean temperature anomalies, *Science*, *324*, 778–781, doi:10.1126/science.1167404.

Flentje, H., H. Claude, T. Elste, S. Gilge, U. Koehler, C. Plass-Duelmer, W. Steinbrecht, W. Thomas, A. Werner, and W. Fricke (2010), The Eyjafjallajokull eruption in April 2010—Detection of volcanic plume using in-situ measurements, ozone sondes and lidar-ceilometer profiles, *Atmos. Chem. Phys.*, *10*, 10085–10092, doi:10.5194/acp-10-10085-2010.

Francis, P. N., M. C. Cooke, and R. W. Saunders (2012), Retrieval of physical properties of volcanic ash using Meteosat: A case study from the 2010 Eyjafjallajokull eruption, *J Geophys Res Atmos*, *117*, D00U09, doi:10.1029/2011JD016788.

Garnier, A., J. Pelon, P. Dubuisson, M. Faivre, O. Chomette, N. Pascal, and D. P. Kratz (2012), Retrieval of cloud properties using CALIPSO imaging infrared radiometer. Part I: Effective emissivity and optical depth, *J Appl Meteorol Climatol*, *51*, 1407–1425, doi:10.1175/JAMC-D-11-0220.1.

Gasteiger, J., S. Gross, V. Freudenthaler, and M. Wiegner (2011), Volcanic ash from Iceland over Munich: Mass concentration retrieved from ground-based remote sensing measurements, *Atmos. Chem. Phys.*, *11*, 2209–2223, doi:10.5194/acp-11-2209-2011.

Giraud, V., J. C. Buriez, Y. Fouquart, F. Parol, and G. Seze (1997), Large-scale analysis of cirrus clouds from AVHRR data: Assessment of both a microphysical index and the cloud-top temperature, *J. Appl. Meteorol.*, *36*, 664–675.

Gu, Y., W. Rose, and G. Bluth (2003), Retrieval of mass and sizes of particles in sandstorms using two MODIS IR bands: A case study of April 7, 2001 sandstorm in China, *Geophys. Res. Lett.*, *30*, 1805, doi:10.1029/2003GL017405.

Gudmundsson, M. T., R. Pedersen, K. Vogfjord, B. Thorbjarnardottir, S. Jakobsdottir, and M. J. Roberts (2010), Eruptions of Eyjafjallajokull Volcano, Iceland, *EOS*, *91*, 190–191.

Guffanti, M., D. J. Schneider, K. L. Wallace, T. Hall, D. R. Bensimon, and L. J. Salinas (2010), Aviation response to a widely dispersed volcanic ash and gas cloud from the August 2008 eruption of Kasatochi, Alaska, USA, *J. Geophys. Res.-Atmos.*, *115*, D00L19, doi:10.1029/2010JD013868.

Hamill, T. M., J. S. Whitaker, and S. L. Mullen (2006), Reforecasts—An important dataset for improving weather predictions, *Bull. Am. Meteorol. Soc.*, *87*, 33–46, doi:10.1175/BAMS-87-1-33-46.

Hannon, S., L. L. Strow, and W. W. McMillan (1996), Atmospheric infrared fast transmittance models: A comparison of two approaches. *Proc. Optical Spectroscopic Techniques and Instrumentation for Atmospheric and Space Research Ii; PROCEEDINGS OF THE SOCIETY OF PHOTO-OPTICAL INSTRUMENTATION ENGINEERS (SPIE); Conference on Optical Spectroscopic Techniques and Instrumentation for Atmospheric and Space Research II*, DENVER, CO, SPIE-INT SOC OPTICAL ENGINEERING, 94–105.

Hansen, J. E., L. D. Travis (1974), Light-scattering in planetary atmospheres, *Space Sci. Rev.*, *16*, 527–610.

Heidinger, A. K., M. J. Pavolonis (2009), Gazing at cirrus clouds for 25 years through a split window. Part I: Methodology, *J Appl Meteorol Climatol*, *48*, 1100–1116, doi:10.1175/2008JAMC1882.1 ER.

Heidinger, A. K., M. J. Pavolonis, R. E. Holz, B. A. Baum, and S. Berthier (2010), Using CALIPSO to explore the sensitivity to cirrus height in the infrared observations from NPOESS/VIIRS and GOES-R/ABI (vol 115, D12299, 2010), *J. Geophys. Res. -Atmos.*, *115*, doi:10.1029/2010JD014461 ER.

Hobbs, P.,L. Radke, J. Lyons, R. Ferek, D. Coffman, and T. Casadevall (1991), Airborne measurements of particle and gas emissions from the 1990 volcanic eruptions of Mount Redoubt, *J. Geophys. Res. -Atmos.*, *96*, 18735–18752, doi:10.1029/91JD01635.

Huang, H., W. Smith, J. Li, P. Antonelli, X. Wu, R. Knuteson, B. Huang, and B. Osborne (2004), Minimum local emissivity variance retrieval of cloud altitude and effective spectral emissivity— Simulation and initial verification, *J. Appl. Meteorol.*, *43*, 795–809, doi:10.1175/2090.1.

Hunt, W. H., D. M. Winker, M. A. Vaughan, K. A. Powell, P. L. Lucker, and C. Weimer (2009), CALIPSO lidar description and performance assessment, *J. Atmos. Ocean. Technol.*, *26*, 1214–1228, doi:10.1175/2009JTECHA1223.1.

ICAO (International Civil Aviation Organization) (2007), Manual on volcanic ash, radioactive material, and toxic chemical clouds (2nd edition). *Doc 9691-AN/954, available at* http://www.paris.icao.int/news/pdf/9691.pdf, 500.

Inoue, T. (1987), A cloud type classification with NOAA 7 split-window measurements, *J. Geophys. Res. -Atmos.*, *92*, 3991–4000.

Jickells, T. D., et al. (2005), Global iron connections between desert dust, ocean biogeochemistry, and climate, *Science*, *308*, 67–71, doi:10.1126/science.1105959.

Johnson, B., et al. (2012), In situ observations of volcanic ash clouds from the FAAM aircraft during the eruption of Eyjafjallajokull in 2010, *J. Geophys. Res. -Atmos.*, *117*, D00U24, doi:10.1029/2011JD016760.

Marenco, F., B. Johnson, K. Turnbull, S. Newman, J. Haywood, H. Webster, and H. Ricketts (2011), Airborne lidar observations of the 2010 Eyjafjallajokull volcanic ash plume, *J. Geophys. Res. -Atmos.*, *116*, D00U05, doi:10.1029/2011JD016396.

Miller, T. P., T. J. Casadevall (2000), Volcanic ash hazards to aviation, Encyclopedia of Volcanoes, H. Sigurdsson, Ed., Academic, San Diego, 915–930.

Neal, C. A., R. G. McGimsey, C. A. Gardner, M. L. Harbin, and C. J. Nye (1994), Tephra-fall deposits from 1992 eruptions of Crater Peak, Mount Spurr Volcano, AK: A preliminary report on distribution, stratigraphy, and composition. The 1992 eruptions of Crater Peak vent, Mount Spurr volcano Alaska, *U S Geol Surv Bull*, *2139*, 65-79.

Newman, S. M., L. Clarisse, D. Hurtmans, F. Marenco, B. Johnson, K. Turnbull, S. Havemann, A. J. Baran, D. O'Sullivan, and J. Haywood

2012, A case study of observations of volcanic ash from the Eyjafjallajokull eruption: 2. Airborne and satellite radiative measurements, *J. Geophys. Res. -Atmos.*, *117*, D00U13, doi:10.1029/2011JD016780.

Parol, F., J. C. Buriez, G. Brogniez, and Y. Fouquart (1991), Information-content of AVHRR channels 4 and 5 with respect to the effective radius of cirrus cloud particles, *J. Appl. Meteorol.*, *30*, 973–984.

Pavolonis, M. J., J. Sieglaff (2010), GOES-R advanced baseline imager (ABI) algorithm theoretical basis document for volcanic ash: Detection and height. Version 2.0., report, 72 pp. *NOAA, Silver Spring, MD [Available at* http://www.goes-r.gov/products/ATBDs/baseline/Aviation_VolAsh_v2.0_no_color.pdf*]*, .

Pavolonis, M. J. (2010), Advances in extracting cloud composition information from spaceborne infrared radiances—A robust alternative to brightness temperatures. Part I: Theory, *J Appl Meteorol Climatol*, *49*, 1992–2012, doi:10.1175/2010JAMC2433.1 ER.

Pavolonis, M. J., W. F. Feltz, A. K. Heidinger, and G. M. Gallina (2006), A daytime complement to the reverse absorption technique for improved automated detection of volcanic ash, *J. Atmos. Ocean. Technol.*, *23*, 1422–1444.

Peyridieu, S., A. Chedin, D. Tanre, V. Capelle, C. Pierangelo, N. Lamquin, and R. Armante (2010), Saharan dust infrared optical depth and altitude retrieved from AIRS: A focus over North Atlantic comparison to MODIS and CALIPSO, *Atmos. Chem. Phys.*, *10*, 1953–1967.

Pollack, J. B., O. B. Toon, and B. N. Khare (1973), Optical properties of some terrestrial rocks and glasses, *Icarus*, *19*, 372-389.

Prata, A. J. (1989a), Infrared radiative-transfer calculations for volcanic ash clouds, *Geophys. Res. Lett.*, *16*, 1293–1296.

Prata, A. J. (1989b), Observations of volcanic ash clouds in the 10–12 μm window using AVHRR/2 data, *Int. J. Remote Sens.*, *10*, 751–761.

Prata, A. J., A. T. Prata (2012), Eyjafjallajokull volcanic ash concentrations determined using spin enhanced visible and infrared imager measurements, *J. Geophys. Res. -Atmos.*, *117*, D00U23, doi:10.1029/2011JD016800.

Prata, A., I. Grant (2001), Retrieval of microphysical and morphological properties of volcanic ash plumes from satellite data: Application to Mt Ruapehu, New Zealand, *Q. J. R. Meteorol. Soc.*, *127*, 2153–2179, doi:10.1256/smsqj.57614.

Prospero, J. M., and P. J. Lamb (2003), African droughts and dust transport to the Caribbean: Climate change implications, *Science*, *302*(5647), 1024–1027 DOI: 10.1126/science.1089915.

Rodgers, C. (1976), Retrieval of atmospheric-temperature and composition from remote measurements of thermal-radiation, *Rev. Geophys.*, *14*, 609–624, doi:10.1029/RG014i004p00609.

Roush, T., J. Pollack, and J. Orenberg (1991), Derivation of mid infrared (5–25 μm) optical-constants of some silicates and palagonite, *Icarus*, *94*, 191–208.

Sandstrom, T., B. Forsberg (2008), Desert dust an unrecognized source of dangerous air pollution? *Epidemiology*, *19*, 808–809, doi:10.1097/EDE.0b013e31818809e0.

Schmehl, K. J., S. E. Haupt, and M. J. Pavolonis (2012), A genetic algorithm variational approach to data assimilation and application to volcanic emissions, *Pure Appl. Geophys.*, *169*, 519-537, doi:10.1007/s00024-011-0385-0.

Schmit, T., M. Gunshor, W. Menzel, J. Gurka, J. Li, and A. Bachmeier (2005), Introducing the next-generation Advanced Baseline Imager on goes-R, *Bull. Am. Meteorol. Soc.*, *86*, 1079-+, doi:10.1175/BAMS-86-8-1079.

Schumann, U., et al. (2011), Airborne observations of the Eyjafjalla volcano ash cloud over Europe during air space closure in April and May 2010, *Atmos. Chem. Phys.*, *11*, 2245-2279, doi:10.5194/acp-11-2245-2011.

Seemann, S. W., E. E. Borbas, R. O. Knuteson, G. R. Stephenson, and H. Huang (2008), Development of a global infrared land surface emissivity database for application to clear sky sounding retrievals from multispectral satellite radiance measurements, *J. Appl. Meteorol. Climatol.*, *47*, 108–123, doi:10.1175/2007JAMC1590.1.

Stohl, A., et al. (2011), Determination of time- and height-resolved volcanic ash emissions and their use for quantitative ash dispersion modeling: The 2010 Eyjafjallajokull eruption, *Atmos. Chem. Phys.*, *11*, 4333–4351, doi:10.5194/acp-11-4333-2011.

Turnbull, K., B. Johnson, F. Marenco, J. Haywood, A. Minikin, B. Weinzierl, H. Schlager, U. Schumann, S. Leadbetter, and A. Woolley (2012), A case study of observations of volcanic ash from the Eyjafjallajokull eruption: 1. In situ airborne observations, *J. Geophys. Res. -Atmos.*, *117*, D00U12, doi:10.1029/2011JD016688.

Turner, D. D. (2008), Ground-based infrared retrievals of optical depth, effective radius, and composition of airborne mineral dust above the Sahel, *J. Geophys. Res. -Atmos.*, *113*, D00E03, doi:10.1029/2008JD010054.

Van de Hulst, H. C. (1980), Multiple Light Scattering, Tables, Formulas, and Applications. Vol. 2, Academic Press, 739 pp.

Vaughan, M. A., K. A. Powell, R. E. Kuehn, S. A. Young, D. M. Winker, C. A. Hostetler, W. H. Hunt, Z. Liu, M. J. McGill, and B. J. Getzewich (2009), Fully automated detection of cloud and aerosol layers in the CALIPSO lidar measurements, *J. Atmos. Ocean. Technol.*, *26*, 2034–2050, doi:10.1175/2009JTECHA1228.1.

Webley, P. W., T. Steensen, M. Stuefer, G. Grell, S. Freitas, and M. Pavolonis (2012), Analyzing the Eyjafjallajokull 2010 eruption using satellite remote sensing, lidar and WRF-Chem dispersion and tracking model, *J. Geophys. Res. -Atmos.*, *117*, D00U26, doi:10.1029/2011JD016817.

Wen, S. M., W. I. Rose (1994), Retrieval of sizes and total masses of particles in volcanic clouds using AVHRR bands 4 and 5, *J. Geophys. Res. -Atmos.*, *99*, 5421–5431.

Wielicki, B., R. Welch (1986), Cumulus cloud properties derived using landsat satellite data, *J. Clim. Appl. Meteoro.*, *25*, 261-276, doi:10.1175/1520-0450(1986)025<0261:CCPDUL>2.0.CO;2.

Winker, D. M., Z. Liu, A. Omar, J. Tackett, and D. Fairlie (2012), CALIOP observations of the transport of ash from the Eyjafjallajokull volcano in April 2010, *J. Geophys. Res. -Atmos.*, *117*, D00U15, doi:10.1029/2011JD016499.

Winker, D. M., et al. (2010), The CALIPSO Mission: A global 3D view of aerosols and clouds, *Bull. Am. Meteorol. Soc.*, *91*, 1211–1229, doi:10.1175/2010BAMS3009.1 ER.

Yu, T. X., W. I. Rose, and A. J. Prata (2002), Atmospheric correction for satellite-based volcanic ash mapping and retrievals using "split window" IR data from GOES and AVHRR, *J. Geophys. Res. -Atmos.*, *107*, 4311.

Zhang, H., W. P. Menzel (2002), Improvement in thin cirrus retrievals using an emissivity-adjusted CO2 slicing algorithm, *J. Geophys. Res. -Atmos.*, *107*, 4327, doi:10.1029/2001JD001037.

Zhang, P., N. Lu, X. Hu, and C. Dong (2006), Identification and physical retrieval of dust storm using three MODIS thermal IR channels, *Global Planet.Change*, *52*, 197-206, doi:10.1016/j.gloplacha.2006.02.014.